NASA CR-159681
PWA-5512-45

NASA

EFFECT OF TIME-DEPENDENT FLIGHT LOADS ON JT9D-7 PERFORMANCE DETERIORATION

JT9D JET ENGINE DIAGNOSTICS PROGRAM

A. Jay and B. L. Lewis

UNITED TECHNOLOGIES CORPORATION
Pratt & Whitney Aircraft Group
Commercial Products Division

Prepared for

NATIONAL AERONAUTICS AND SPACE ADMINISTRATION

NASA Lewis Research Center
Contract NAS3-20632

1. Report No.	2. Government Accession No.	3. Recipient's Catalog No.
NASA CR-159681		

4. Title and Subtitle	5. Report Date
Effect of Time-Dependent Flight Loads on JT9D-7 Performance Deterioration	August 21, 1979
	6. Performing Organization Code

7. Author(s)	8. Performing Organization Report No.
A. Jay and B. L. Lewis	PWA-5512-45
	10. Work Unit No.

9. Performing Organization Name and Address	11. Contract or Grant No.
UNITED TECHNOLOGIES CORPORATION Pratt & Whitney Aircraft Commercial Products Division East Hartford, Connecticut 06108	NAS3-20632
	13. Type of Report and Period Covered Contractor Report

12. Sponsoring Agency Name and Address	14. Sponsoring Agency Code
NATIONAL AERONAUTICS AND SPACE ADMINISTRATION Lewis Research Center Cleveland, Ohio 44135	

15. Supplementary Notes

Project Manager: Joseph A. Ziemianski
Project Engineer; Edward G. Stakolich
NASA Lewis Research Center; Cleveland, Ohio 44135

16. Abstract

This report presents the results of a modal transient analysis of the engine/- aircraft system. The response of the JT9D to analytically simulated vertical gusts and landings was predicted using a NASTRAN (NASA STRUCTURAL ANALYSIS) finite element mathematical model of the JT9D/747 propulsion system.

The NASTRAN finite element model of the propulsion system included engine structural models of the fan, low-/high-pressure compressors, diffuser/turbine cases, and high-/low-pressure rotors, as well as nacelle models of the inlet cowl, tailcone, and wing pylon.

The analysis conducted predicts that an insignificant level of JT9D-7 performance deterioration would occur due to a typical vertical gust encounter or a typical revenue service landing. Analysis of a high sink rate landing with a heavy fuel load indicates the possibility of local wear, however, the lack of an accurate dynamic rotor/seal interference model precludes an accurate quantitative evaluation of performance change for this once-per-airframe-life event.

17. Key Words (Suggested by Author(s))	18. Distribution Statement
Modal Transient Analysis Time Dependent Flight Loads Performance Deterioration	

19. Security Classif. (of this report)	20. Security Classif. (of this page)	21. No. of Pages	22. Price*
Unclassified	Unclassified	80	

* For sale by the National Technical Information Service, Springfield, Virginia 22161

PREFACE

The requirements of NASA Policy Directive NPD 2220.4 (September 14, 1970) regarding the use of SI Units have been waived in accordance with the provisions of paragraph 5d of that Directive by the Director of Lewis Research Center.

TABLE OF CONTENTS

LIST OF ILLUSTRATIONS

LIST OF ILLUSTRATIONS (Cont'd.)

LIST OF ILLUSTRATIONS (Cont'd.)

LIST OF TABLES

SECTION 1.0

SUMMARY

A jet engine's efficiency is strongly dependent upon clearances between rotating blades and the corresponding stationary gas-path seals. Analytical studies examining the effects of various flight cycle loads upon powerplant clearances suggest that rotor/seal interferences contribute significantly to the short-term performance deterioration exhibited by high bypass propulsion systems. In prior analytical studies (1)*, flight cycle loads were treated in a quasi-steady, static manner, even though some flight cycle loadings are decidedly dynamic in nature. Typical examples of dynamic flight loads are gust encounters and hard landings. To better quantify the structural response of the JT9D in the flight environment, a modal transient analysis of the airframe/propulsion system has been performed. The response of the JT9D-7 to analytically simulated vertical gusts and landing touchdowns was predicted using an existing NASTRAN (NASA STRUCTURAL ANALYSIS) finite element mathematical model of the JT9D/747 propulsion system.

The NASTRAN finite element model of the propulsion system included engine structural models of the fan, low-/high-pressure compressors, diffuser/turbine cases, and the high-/low-pressure rotors, as well as nacelle models of the inlet cowl, tailcone, and wing pylon. A modal synthesis technique was used to extract the integrated propulsion/airframe system natural frequencies. Calculated frequencies were in good agreement with available test data. Transient response calculations included rotor gyroscopic terms and modal damping. Time dependent powerplant displacement data was related to performance characteristics using a postprocessing system allowing clearance changes to be graphically reviewed and recorded at various time points during the load transients.

The analysis conducted predicts that an insignificant level of JT9D-7 performance deterioration would occur due to a once-per-flight** vertical gust encounter (0.04 percent ΔTSFC at cruise) or a typical revenue service landing (0.2 percent ΔTSFC at cruise). These results strengthen the conclusions from the previous study (1) that steady aerodynamic pressure loads are probably responsible for the bulk of the TSFC loss predicted to be caused by flight loads. The results also indicate that the quasi-steady state approach to flight loads modeling is adequate to investigate the factors important to the deterioration

---

* Numbers in ( ) indicate references in Section 9.0.

** The once-per-flight gust encounter simulates response of the aircraft to a column of rising air and represents the maximum effects of air turbulence expected to occur during an average flight.

process, especially the short-term aspect. Analysis of a high sink rate landing with a heavy fuel load indicates the possibility of local wear, however, the lack of an accurate dynamic rotor/seal interference model precludes an accurate quantitative evaluation of performance change for this once-per-airframe-life event. The lack of suitable flight dynamic load data to conduct other analytical studies of the dynamic load events during a typical flight cycle suggests the need for a flight test program specifically designed to obtain propulsion system load data. The flight test program suggested could expand the empirical base for calibration of the various analytical studies conducted.

SECTION 2.0

INTRODUCTION

The deterioration of a jet engine's fuel efficiency can be generally attributed to erosion, contamination of airfoils, thermal distortion of hot section parts, and increases in clearances between rotating blades and the corresponding outer air seals. The high bypass propulsion systems powering today's wide body aircraft fleet also suffer a short-term deterioration process with losses of about 1 percent in TSFC during the first few flights that is undesirable in light of current fuel costs. To combat high bypass engine deterioration, a study to understand the deterioration mechanisms has been conducted at Pratt & Whitney Aircraft under the Engine Diagnostics (ED) part of the Engine Component Improvement (ECI) program. The ECI program is an element of the NASA sponsored Aircraft Energy Efficiency (ACEE) program which is directed toward reducing fuel consumption of commercial air transports. One task of this study has been the utilization of a structural model of the JT9D-7 to analytically examine the potential effects of flight induced loads on performance deterioration.

Previous analytical studies (1) treating flight induced propulsion system loads in a quasi-steady manner suggest the primary cause of short-term deterioration to be the increase in operating clearances resulting from flight load induced rotor/seal interference. The static analysis results are in good agreement with engine performance data in the low cycle (1 to 300 flight) regime, as shown in Figure 1.

Although the quasi-steady approach to the flight loads spectrum appears to provide an adequate simulation of the clearance induced deterioration process, some flight loads are inherently time dependent in nature, raising the possibility of significant dynamic effects in the rotor/seal interference process. The transient dynamic analysis was conducted to increase the knowledge of the structural behavior of the JT9D-7/747 propulsion system and to relate this knowledge to seal rub patterns and performance characteristics exhibited by testing and inspection of engines from typical revenue service.

The finite element model of the JT9D-7/747 employed for this study was previously developed by Pratt & Whitney Aircraft (P&WA) and the Boeing Commercial Airplane Company (BCAC). The finite element model is shown in Figure 2.

The intent of the transient dynamic analysis of the JT9D was to examine specific load events of a typical flight profile examined in the quasi-steady analysis, Figure 3, and determine if the associated dynamic effects on seal wear and performance were substantial. These events are a vertical wind gust encounter and two types of landings. In performing the quasi-steady analysis, dynamic amplification factors were used in projecting peak loads, therefore, an evaluation of the amplification

factors was sought. Since the dynamic approach requires considerably more resources, an evaluation of the relative merits of static versus dynamic flight loads modeling was a secondary objective of the analysis effort.

SECTION 3.0

ANALYTICAL OVERVIEW

3.1 INTEGRATED PROPULSION SYSTEM MODEL DESCRIPTION

The NASTRAN finite element model of the JT9D/nacelle structure utilized in these studies was identical to that employed in the steady loads analysis. Engine cases are modeled primarily with quadrilateral plate elements with enhanced membrane capabilities. Triangular plate elements are used in areas of mesh transitioning or irregular geometry. The high-/low-pressure rotor spools are beam-lumped mass model duplicates of those employed in standard critical speed design analysis of the JT9D.

The model is substructured by component regions consisting of the fan/low-pressure compressor, high-pressure compressor, diffuser/turbine cases, the high-/low-pressure rotors, and the inlet cowl, tailcone, and wing pylon structures. Since the wing is not modeled, the structure was considered symmetric about a vertical plane and one-half of the structure is modeled as shown in Figure 4. This half model of the propulsion system contains approximately 11,000 degrees of freedom. A summary of the model is given in Table I.

3.2 MODAL ANALYSIS CONSIDERATIONS

The modal transient approach was selected as the analysis procedure due to its economic superiority over the direct integration technique for this problem. It also provided physical insight into the analysis regarding the frequency spectrum, participation of the various modes in the response, and led to the convenient use of modal damping.

In general the standard NASTRAN transient analysis package was utilized. Some modifications were required to the basic NASTRAN computational procedures, however, due to the following considerations:

- Desired utilization of structural symmetry
- Modal damping
- Time-dependent enforced displacements
- Nonstandard dynamic reduction procedure
- Gyroscopic effects

An overview of the impact of these considerations on the transient response formulation follows.

MODAL TRANSIENT FORMULATION

The modal transient formulation is available in many references, (3), (4), and will only be outlined here. The equation to be solved was:

$$[M]\{\ddot{x}\} + [C]\{\dot{x}\} + [G]\{\dot{x}\} + [K]\{x\} = \{F(t)\} \qquad \text{Eqn. 1}$$

where $[M]$ = structure mass matrix

$[C]$ = structure viscous damping matrix

$[G]$ = rotor gyroscopic matrix

$[K]$ = structure stiffness matrix

Since the model is substructured the matrices of Equation 1 represent the assembled contributions from the various substructures. The zero speed, undamped modal matrix of Equation 1 (ϕ_N) was then formed.

$$[M]\{\ddot{x}\} + [K]\{x\} = \{0\} \qquad \text{Eqn. 2}$$

$$\{x\} = \{x_0\} e^{i\omega t} \qquad \text{Eqn. 3}$$

$$\{[M]\omega^2 + [K]\}[\phi_N] = \{0\} \qquad \text{Eqn. 4}$$

The modal matrix ϕ_N was mass normalized and the standard modal transformation applied to Equation 1.

$$\{x\} = [\phi_N]\{\eta\} \qquad \text{Eqn. 5a}$$

$$[\phi_N]^T[M][\phi_N]\{\ddot{\eta}\} + [\phi_N]^T[C][\phi_N]\{\dot{\eta}\} + [\phi_N]^T[G][\phi_N]\{\dot{\eta}\} + [\phi_N]^T[K][\phi_N]\{\eta\} = [\phi_N]^T\{F(t)\} \qquad \text{Eqn. 5b}$$

$$[\hat{M}]\{\ddot{\eta}\} + [\phi_N]^T[C][\phi_N]\{\dot{\eta}\} + [\phi_N]^T[G][\phi_N]\{\dot{\eta}\} + [\hat{K}]\{\eta\} = [\phi_N]^T\{F(t)\} \qquad \text{Eqn. 6}$$

where $[\hat{M}]$ = generalized mass $= [\hat{I}]$

$[\hat{K}]$ = generalized stiffness $= [\hat{\omega}^2]$

Damping in the propulsion system is developed in numerous ways. Bolted flanges, case/strut attachments, mount points, design dampers, and inherent structural damping are some examples. In a structure with the complexity of the JT9D, an accurate assessment of the discrete damping matrix $[C]$ is impractical if not impossible. Consequently, as in many

engineering applications, modal damping was employed. The matrix product $[\phi_N]^T [C] [N]$ thereby is reduced to diagonal form with each entry proportional to the critical damping factor for the respective mode. Modal damping factors may be either obtained from test data or assigned values consistent with prior experience.

3.4 GYROSCOPIC CONSIDERATIONS

With the incorporation of modal damping, the equations of motion are generally uncoupled, leading to substantial computational savings. The gyroscopic behavior of the rotors, characterized by the matrix $[G]$, produces effects which couple the equations of motion. The physical significance of this behavior is that the symmetric and antisymmetric components of motion are coupled and the half model used in the quasi-steady loads analysis can no longer directly describe the powerplant structural response.

A typical stage of the rotor system and the associated analysis coordinate system is shown in Figure 5. Each stage of the rotor behaves as a gyroscope, tending to resist rotation in any direction other than the axis of rotation. Mathematically the gyroscopic behavior of each stage is defined by Equation 7.

$$\begin{Bmatrix} F_x \\ F_y \\ F_z \\ M_x \\ M_y \\ M_z \end{Bmatrix} = \begin{bmatrix} 0 & 0 & 0 & 0 & 0 & 0 \\ 0 & 0 & 0 & 0 & 0 & 0 \\ 0 & 0 & 0 & 0 & 0 & 0 \\ 0 & 0 & 0 & 0 & -I_p\Omega & 0 \\ 0 & 0 & 0 & I_p\Omega & 0 & 0 \\ 0 & 0 & 0 & 0 & 0 & 0 \end{bmatrix} \begin{Bmatrix} \dot{x} \\ \dot{y} \\ \dot{z} \\ \dot{\theta}x \\ \dot{\theta}y \\ \dot{\theta}z \end{Bmatrix} \qquad \text{Eqn. 7}$$

where: I_p = Polar Mass Moment of Inertia of Stage

Ω = Rotor Rotational Velocity

To aid in the physical interpretation of the large amounts of displacement data, it was deemed desirable to maintain the symmetric/antisymmetric displacement representation of the structure. This representation was preserved by using symmetric and antisymmetric half models of the structure and coupling the two representations through the gyroscopic matrix. This technique is applicable only because the coupling occurs along the plane of structural symmetry. Using this approach Equation 1 may be rewritten as follows:

$$\begin{bmatrix} M_S & 0 \\ 0 & M_A \end{bmatrix} \begin{Bmatrix} \ddot{x}_S \\ \ddot{x}_A \end{Bmatrix} + \begin{bmatrix} C_S & 0 \\ 0 & C_A \end{bmatrix} \begin{Bmatrix} \dot{x}_S \\ \dot{x}_A \end{Bmatrix} + \begin{bmatrix} 0 & G_{SA} \\ -G^T_{SA} & 0 \end{bmatrix} \begin{Bmatrix} \dot{x}_S \\ \dot{x}_A \end{Bmatrix}$$

$$+ \begin{bmatrix} K_S & 0 \\ 0 & K_A \end{bmatrix} \begin{Bmatrix} x_S \\ x_A \end{Bmatrix} = \begin{Bmatrix} F_S(t) \\ F_A(t) \end{Bmatrix} \qquad \text{Eqn. 8}$$

In Equation 8 the subscripts S and A refer to symmetric and antisymmetric displacement representations of the half model, respectively. These matricies were generated using the half model with symmetric or antisymmetric boundary conditions along the plane of structural symmetry.

Equation 8 was then partitioned into symmetric and antisymmetric representations and the zero speed modal matrix formed, per Equation 4.

$$[\phi_N] = \left[\begin{array}{c} \phi_{SN} \\ \hline \phi_{AN} \end{array}\right] \qquad \text{Eqn. 9}$$

Using the mass normalized modal matrix, the modal transformation is performed on Equation 8, leading to the mathematical representation of the JT9D-7 response.

$$\begin{bmatrix} \ddots & 0 \\ M_S & \\ & \ddots \\ 0 & M_A \end{bmatrix} \begin{Bmatrix} \ddot{\eta}_S \\ \ddot{\eta}_A \end{Bmatrix} + \begin{bmatrix} \ddots & 0 \\ C_S & \\ & \ddots \\ 0 & C_A \end{bmatrix} \begin{Bmatrix} \dot{\eta}_S \\ \dot{\eta}_A \end{Bmatrix} \qquad \text{Eqn. 10}$$

$$+ \begin{bmatrix} \phi_{SN} \\ \hline \phi_{AN} \end{bmatrix}^T \begin{bmatrix} 0 & G_{SA} \\ -G^T_{SA} & 0 \end{bmatrix} \begin{bmatrix} \phi_{SN} \\ \hline \phi_{AN} \end{bmatrix} \begin{Bmatrix} \dot{\eta}_S \\ \dot{\eta}_A \end{Bmatrix}$$

$$+ \begin{bmatrix} \ddots & 0 \\ K_S & \\ & \ddots \\ 0 & K_A \end{bmatrix} \begin{Bmatrix} \eta_S \\ \eta_A \end{Bmatrix} = \begin{bmatrix} \phi_{SN} \\ \hline \phi_{AN} \end{bmatrix}^T \begin{Bmatrix} F_S(t) \\ F_A(t) \end{Bmatrix}$$

where: η_S = symmetric modal participation vector
η_A = antisymmetric modal participation vector

3.5 DYNAMIC REDUCTION CONSIDERATIONS

The half model of the JT9D powerplant contains approximately 11,000 degrees of freedom. In preserving the symmetric/antisymmetric displacement representation the problem size was doubled. For such a problem size, it is economically impractical to extract the modes required for the modal analysis, consequently some form of dynamic reduction was

necessary to reduce the problem size. The type and level of reduction performed can have an adverse effect upon frequency and particulaly modal data. Since the quality of any modal transient analysis is governed by the frequency and modal data used, the dynamic reduction performed must be done judiciously.

Several reduction schemes are commonly used, and four types were examined for use in this analysis. The types examined were:

- o Mass Lumping followed by Static Condensation
- o Guyan Reduction
- o Distributed Parameter Systems
- o Fixed Boundary Modal Synthesis Techniques

Both mass lumping and Guyan reduction have been extensively used. Studies with these techniques on shell structures have indicated that substantial modal errors may be induced even for the low modes of the structure when heavy levels of reduction are utilized. Distributed parameter systems include the FEER eigenvalue technique (5) and the generalized dynamic reduction procedure of MacNeal (7). Both of these techniques are relatively new and the latter has shown promising performance for some engine hardware applications. At the initiation of this analysis, however, no evaluation had been made using these techniques for shell structures. Consequently both techniques were ruled out, although subsequent studies have indicated these to be promising techniques for future analysis.

A procedure developed by Craig and Bampton (6) was found to produce excellent results for shell structures and to be readily adaptable to the NASTRAN program. In this procedure, both physical and modal degrees of freedom are used to describe the structure. The modal variables are generated by fixing each substructure at its interfaces with other substructures and extracting the "fixed boundary modes" of the substructure. Displacement compatability is then required at the various substructure boundaries to form the system description, Equation 8. A brief theoretical overview of the Craig and Bampton technique follows.

Each substructure is partitioned into internal and boundary degrees of freedom per Equation 11. The boundary set must include all freedoms common with other substructures.

$$\begin{bmatrix} M_{BB} & 0 \\ 0 & M_{II} \end{bmatrix} \begin{Bmatrix} \ddot{x}_B \\ \ddot{x}_I \end{Bmatrix} + \begin{bmatrix} K_{BB} & K_{BI} \\ K^T_{BI} & K_{II} \end{bmatrix} \begin{Bmatrix} x_B \\ x_I \end{Bmatrix} = \begin{Bmatrix} 0 \\ 0 \end{Bmatrix} \quad \text{Eqn. 11}$$

The fixed boundary frequencies and mode shapes ($\{\phi_I\}$) of each substructure are then extracted from equation 12.

$$\omega^2 \left[M_{II}\right] \left\{\phi_I\right\} = \left[K_{II}\right] \left\{\phi_I\right\} \qquad \text{Eqn. 12}$$

The final displacements of each substructure are then expressed as a linear combination of the boundary induced displacements and the participation of the various fixed boundary modes.

$$\begin{Bmatrix} X_{boundary} \\ X_{internal} \end{Bmatrix} = \left[\begin{array}{c|c} I & 0 \\ \hline \phi^c & \phi_I \end{array}\right] \begin{Bmatrix} P_b \\ P_I \end{Bmatrix} \qquad \text{Eqn. 13}$$

where:
- P_b = substructure boundary displacements
- P_I = participation factors for various substructure fixed boundary modes
- $\{\phi^c\}$ = Displacement of internal degree of freedom due to boundary displacement, i.e.,

$$\{\phi^c\} = -[K_{II}]^{-1} \cdot [K_{IB}]$$

Since each modal degree of freedom ($[P_I]$) represents a physically meaningful displacement pattern for the substructure, this technique is generally more efficient than Guyan reduction where one freedom typically represents a rather arbitrary displacement pattern. Computationally, the Craig and Bampton technique compares favorably with Guyan reduction.

In addition to the effectiveness and simplicity of the Craig and Bampton technique, the procedure also provides intermediate checks on the structural model and analysis.

- o By extracting the fixed boundary modes of the substructures, the analyst is given a means of checking the structural model early in the assembly phase.
- o The frequency spectrum of the fixed boundary modes provides insight into the likely participation of the various modes if the harmonic content of the transient loads is known.
- o The fixed boundary mode procedure provides a means for further reducing the dynamic problem size. If the fixed boundary frequencies are considerably higher than the transient forcing functions, the fixed boundary modes may simply be restrained from participating.

The need for carefully managing the dynamic reduction procedure is illustrated by the simply supported shell of Figure 6. The results of the second bending, first harmonic frequency for this structure are shown in Figure 7, comparing the Craig and Bampton procedure with a

Guyan reduction scheme similar to the one employed in the original normal modes analysis (2). As can be seen, the approach utilized leads to a substantial improvement in the modal data for this case.

3.6 ENFORCED DYNAMIC DISPLACEMENTS

In the quasi-steady analysis of the JT9D/747, the wing pylon was attached to a rigid mount. In dynamic analyses, the powerplant displacements are due primarily to the elastic response of the aircraft wing. Consequently, a procedure must be available whereby time dependent displacement histories may be enforced on the model. These displacement histories are products of the airframe aeroelastic analysis and are defined for all six motions of the wing elastic axis at its intersection with the pylon centerplane.

In NASTRAN, enforced dynamic displacements are applied through a "large mass" or "acceleration generator". A mass several orders of magnitude larger than the structure is assigned to each degree of freedom where time dependent displacements are to be applied. The large masses result in essentially zero frequency, rigid body modes of the structure. These rigid body modes may then be excited by forces producing accelerations that integrate to the desired displacement histories.

In the evaluation of this technique prior to this analysis, essentially exact results were obtained for simple spring-mass systems subject to the wing aeroelastic displacement histories. However in physical modeling of the JT9D/747 and other structures, this method has been unable to reproduce the enforced dynamic displacements. The exact error involved for the JT9D analysis will be discussed later, however, the lack of an accurate technique for enforcing time dependent displacements lowered the quantitative credibility of the performance evaluations obtained for the simulated landing events.

SECTION 4.0

DYNAMIC LOADS AND DAMPING DESCRIPTIONS

The computational costs involved and limited availability of airframe aerolastic data permitted evaluation of only two flight load conditions in the mission profile analyzed in the quasi-steady analysis. The two points from the steady loads spectrum which generate the most interesting dynamic load conditions are gust encounters and landing touchdowns. Both are inherently dynamic in nature and are described in a relatively short time period. For these flight conditions, BCAC generated aeroelastic data for a vertical gust and four different landing sequences. The aerolastic data employed reflects the behavior of the wing at the outboard engine location. The four landing sequences represent variations in aircraft gross weights, fuel loads, and sink rates. With this information, three separate dynamic analyses were conducted. The conditions analyzed corresponded to a once-per-flight vertical gust, a typical revenue service landing, and a once-per-airplane-life landing.

4.1 VERTICAL GUST DESCRIPTION

The vertical gust encounter analyzed was a once-per-flight value of 10 feet/second at the following flight condition:

- Altitude 22,100 ft
- Gross Weight 730,400 lb
- Mach Number 0.875
- True Airspeed 897.8 ft/sec

Although wing displacement data were available for 1.5 seconds, only the first 0.75 second was judged to be valid by the airframe manufacturer. For the gust condition, cowl aerodynamic load histories were also generated by BCAC and imposed upon the NASTRAN model.

The coordinate system defining the directions used for wing displacement histories is shown in Figure 8. The time histories for vertical, lateral, and longitudinal displacements along with pitch, yaw, and roll values are shown graphically in Figures 9 through 14, respectively. The incremental vertical aerodynamic load history created by the changing cowl angle of attack is shown in Figure 15.

4.2 LANDING EVENT DESCRIPTIONS

Of the four landings described by BCAC, the following two were chosen for analysis.

- Gross Weight 490,000 lb
  Fuel Weight 43,000 lb
  Sink Rate 3 ft/sec

o	Gross Weight	449,000 lb
	Fuel Weight	118,000 lb
	Sink Rate	10 ft/sec

The first case represents a typical revenue service profile landing. The second, a once-per-airframe-life event with a high fuel load and an extremely high sink rate. This case represents possibly the most severe dynamic event occuring during an airframe life. In actual flight testing this condition has been extremely difficult to achieve.

For the landing events analyzed, the inlet aerodynamic forces were estimated by BCAC to be negligible and were neglected. Consequently, the dynamic loads for the landing simulations consisted only of the enforced wing displacements. The displacement histories for the two landings are shown in Figures 16 through 27.

4.3 CALCULATION AND ASSESSMENT OF DAMPING QUANTITIES

To extract modal damping factors for the propulsion system, accelerometer data from Pratt & Whitney Aircraft's flight testing was reviewed. Although the flight test aircraft was a B-52, the pylon and engine structures for JT9D flight testing are similar to the JT9D/747 system modeled in this analysis. The particular test sequence utilized concerned verification of the aircraft flight envelope by recording the aircraft response to various control surface inputs. Accelerometer data from various points on the powerplant were also recorded.

A high speed transient analysis of the powerplant accelerometer data was conducted and the following frequencies identified.

2.2	Hz	25.	Hz
5.2	Hz	31.	Hz
10.2	Hz	58.	Hz
14.6	Hz	60.4	Hz

This frequency spectrum is similar to that extracted from the current analysis as shown in Table VIII. The trace of the higher modes was of insufficient strength or duration for constructing accurate amplitude versus time histories. Consequently a 12 Hz band filter was utilized and an amplitude versus time history was created for the first mode of the system (2.2 Hz). Using Equation 14 in conjunction with the accelerometer data, several calculations of damping factors were made and averaged. The resulting critical damping factor was 6.06 percent which was applied to all modes used in the modal transient analysis.

$$\delta = \frac{\log A_0/A_n}{\left\{1.862\ N^2 + (\log A_0/A_n)^2\right\}^{1/2}} \qquad \text{Eqn. 14}$$

where:

δ = critical damping ratio

A_0 = amplitude of wave at time t_1

A_n = amplitude of wave after n^{th} cycle

N = number of cycles

Because of the many sources of damping in the propulsion system and pylon structures, the value of 6 percent critical damping was felt to be reasonable for the lower modes of the system. In addition, the dynamic response of the propulsion system to the loads being analyzed was anticipated to be dominated by the lower modes of the system. Consequently, an accurate assessment of a typical lower mode damping factor was felt to be more important than for higher modes. During the coarse of the hard landing analysis, damping studies were performed for critical damping factors of 3, 6, and 12 percent with no substantial change in the rub patterns or performance deficit calculated.

SECTION 5.0

DYNAMIC RUB STRIP INTERFERENCE MODEL

5.1 ROTOR/SEAL CLEARANCE CHANGE METHODOLOGY

The process by which rotor/gas-path seal clearances were calculated during the transient analysis is shown schematically in Figure 28. The position of the shaft center with respect to the case centerline is computed for each stage at each time point in the analysis. The change in the distance between the deflected and undeflected rotor/case locations was then calculated at various points, typically every 12 degrees around the seal circumference. These distance changes may be compared with the available clearance for each stage at the various circumferential locations to determine if the clearances are opening, closing, or if interference (rubbing) has occurred for that time point. The available clearance at any time point consists of the base-line clearances designed into the powerplant at a particular performance point (1), any wear incurred prior to the dynamic event as determined in the quasi-steady analysis, and any wear incurred as a result of previous time points in the dynamic analysis.

Physically the interference sequence is a complex event, as there is an additional dynamic force generated on the rotor as contact with the seal occurs. This force cannot economically be modeled in a linear dynamic analysis. Consequently, the dynamic interference model is considered adequate for small interferences, but not quantitatively accurate for large interference values.

5.2 TRANSIENT STEP SIZE CONSIDERATIONS

In selecting the transient step size there were three governing considerations:

- In a modal transient analysis, the step size selected directly affects the numerical results through the stability of higher mode contributions.
- The time step must be small enough to track the orbit of each rotor in order to provide accurate circumferential clearance/interference information.
- Economic factors and computing resources.

The relationship between a given time step (Δt) and the error induced for a participating mode of frequency (ω) can be expressed by Equation 15 (4).

$$\frac{A_f}{A_e} = 1 + \frac{1}{8}\omega^2 \Delta t^2 \qquad \text{Eqn. 15}$$

where:
- A_f = computed amplitude of modal contribution from mode with frequency ω
- A_e = amplitude of modal contribution from exact solution
- ω = circular frequency
- Δt = time step size

It was required that there be less than 5 percent error in a mode with a frequency of 100 Hz, and Equation 15 was used to yield a time step of 0.001 second.

For the dynamic analysis it was anticipated that the propulsion system response would be governed by the wing displacements. As can be seen from Figures 9 through 14 and 16 through 27, these displacements are primarily of relatively low frequency content when compared to the computed integrated propulsion system frequency spectrum (Table VIII). Consequently, the modes in the 0 to 20 Hz range were expected to have the highest participation factors. If, in the modal analysis, modes to the 100 Hz level were retained, this would provide a 5 to 1 frequency margin over the anticipated primary participation range and would also provide adequate coverage for higher modes which might be excited in the hard landing, or whose static contributions were required.

The 0.001 second transient time step provides 8.264 examinations per revolution of the high-pressure spool rotor and 17.85 of the low-pressure spool rotor at cruise conditions. This is considered to be the minimum acceptable number of evaluations for the high-pressure spool rotor, however, this leads to prohibitly large computer run times. To allow this time step to be utilized, velocity and acceleration calculations were deleted from the NASTRAN calculations for the various substructures, saving approximately five hours of computer time per dynamic analysis. This procedure limits the amount of data generated but does not affect the accuracy of the displacement calculations which are used in assessing performance.

SECTION 6.0

JT9D/747 TRANSIENT DYNAMIC RESULTS

To summarize the information of the previous sections, the following steps were performed in the analysis of the three dynamic flight conditions.

- The symmetric and antisymmetric fixed boundary modes of each substructure were computed, and the dynamic mass and stiffness properties of the various substructures were formed. The rotor substructure was reduced using Guyan reduction.

- Substructure matricies were assembled, forming Equation 8, and the zero speed modes of the integrated propulsion system were extracted.

- Modes of the system up to 100 Hz were retained for a modal transient response of the BCAC-supplied dynamic loads with a transient step size of 0.001 second. The enforced dynamic displacements of the wing elastic axis were compared to the NASTRAN resultants as a solution check.

- The displacements of the individual substructures were computed at the various time points and the data used to construct a performance evaluation via the engine performance post-processor computer program.

- An evaluation of the results obtained was conducted, and an assessment of the results was made.

6.1 SUBSTRUCTURE FIXED BOUNDARY MODE SPECTRUMS

The fixed boundary modes of the cowl, fan, high-pressue compressor, turbine, tailcone, and pylon substructures are given in Tables II through VII, respectively. As can be seen, the fixed boundary spectrums of all substructures exhibit few modes below 100 Hz.

Frequency and modal convergence studies conducted with the Craig and Bampton procedure have shown that acceptable propulsion system modal convergence is obtained for a fixed boundary frequency cutoff of three-to-one over the highest mode of interest. A 100 Hz cutoff value for the transient response demands that fixed boundary modes be calculated to at least the 300 Hz level. Examination of Tables II through VII shows the lowest fixed boundary cutoff frequency to be 484 Hz for the fan symmetric modes.

6.2 INTEGRATED PROPULSION SYSTEM FREQUENCIES

The frequency spectrum calculated for the JT9D/747 propulsion system is shown in Table VIII. Modal descriptions and correlating test data are given where available. The amount of test data is small but comparisons with existing test data are considered excellent. The frequencies shown in Table VIII were calculated using a fixed boundary mode cutoff frequency of 600 Hz, as were the frequencies and mode shapes used in the modal transient analysis.

To investigate the stability of the propulsion system frequencies with respect to various fixed boundary truncation levels, the frequency calculation process was repeated using truncation levels of 500 and 400 Hz. The largest frequency change in the first 75 calculated modes (214 Hz) was 0.2 percent. The largest change in the 200 frequencies calculated was 1.6 percent in the 91st mode. Since fewer than 60 modes were utilized in the transient analysis, the frequency and modal data were judged to be numerically acceptable.

6.3 ENFORCED DYNAMIC DISPLACEMENT BEHAVIOR

Figures 29 through 34 compare the BCAC-generated wing displacement histories with those resulting from the NASTRAN program for the once-per-flight vertical gust. Although some deviation is noted, the gust solution is judged to be unaffected and the transient displacements representative of this flight event.

Figures 35 through 40 compare the input wing displacement histories with those returned through the analysis for the revenue and hard landing events. As can be seen, the deviation for these events is larger than for the vertical gust encounter. With the exception of the vertical displacements, however, these results are considered satisfactory. In particular, the pitch motions are well behaved. Since the gyroscopic effects are directly proportional to the pitch velocities, this portion of the dynamic loading is felt to be accurately analyzed.

A spectral analysis of the vertical displacement data for the landing simulations revealed unexpected high frequency (above 10 Hz) participation in the aeroelastic response. It is believed that this high frequency noise is partially responsible for the deviation in the vertical response history. Although numerical filtering of the data is possible, no means exist to assess the correctness of the displacement data resulting from the filtering process with respect to actual airframe response.

An evaluation of the vertical displacement histories resulting from the landing simulations reveals incremental vertical g loadings that are consistently higher than the BCAC aeroelastic analysis. Since the primary effect of motion in the vertical direction is to induce inertia

loadings on the case and rotors, it is felt that the conditions analyzed are conservative with respect to those dictated by the aeroelastic analysis.

6.4 VERTICAL GUST RESULTS

The available clearance for each stage at the time of the gust encounter includes the baseline design clearances at cruise plus any wear from interference which has occurred at previous points in the flight cycle. The prior wear results mainly from aerodynamic loads on the inlet during take-off and climb and are taken from the quasi-steady analysis (1).

The circumferential rub map resulting from the once-per-flight vertical gust is shown in Table IX. The resulting TSFC deficits associated with this wear are 0.04 percent at cruise and 0.07 percent for the sea level take-off point. These TSFC changes are computed from tables of average clearance change versus percent change in TSFC (1).

6.5 REVENUE SERVICE AND HARD LANDING RESULTS

The circumferential rub patterns resulting from the revenue service and hard landing simulations are shown in Tables X and XI, respectively. The predicted performance deterioration associated with the revenue landing is about 0.2 percent at cruise. The corresponding value for the hard landing is about one percent and is believed to be excessive due to the lack of a suitable dynamic interference model of the interaction between blade tips and outer air seals.

SECTION 7.0

ASSESSMENT OF TRANSIENT DYNAMIC ANALYSIS RESULTS

One problem associated with large scale dynamic analysis is the generation of a large quantity of data which does not readily yield to a comprehensive evaluation. For this analysis, approximately 99 million pieces of data were generated in the process of developing the three performance deterioration values for characterizing the gust and landing simulations.

An assessment of the validity of these results can be made through an engineering evaluation of various intermediate results of the analysis. For the JT9D-7 study, the computed frequency spectrum, performance deterioration values and associated seal wear patterns, and the modal participation data provides check points for examining the analysis.

Empirical data for verification of the computed frequency spectrum (Table VIII) is somewhat limited. The frequencies obtained, however, were in good agreement with the available test data and calculations made using the standard Pratt & Whitney Aircraft design analysis tools. Table XII summarizes the available calibration data.

In addition to these sources of verification, various other computed frequencies and mode shapes were found to be in good agreement with design studies employing body of revolution, shell of revolution, or beam modeling of miscellaneous engine components. On the basis of the available means of correlation, the computed propulsion system frequencies were believed accurate, providing confidence in the basic elastic and mass modeling of the structures.

In light of service experience, the once-per-flight vertical gust was expected to result in negligible performance loss. The analysis supports this experience, predicting a change in TSFC of 0.04 percent from the gust simulation. Examination of the predicted seal wear pattern from the gust encounter (Table IX) indicates the primary response to be gyroscopic behavior of the fan from the wing pitching motions. Pitching of the low-pressure compressor results in predicted seal wear in the last LPC stage. The analysis locations of seal rubs for the fan and low-pressure compressor are offset 180 degrees as expected. Inertia forces during the gust encounter are not sufficient to induce seal wear at the top or bottom of the other air seals, supporting the results of the quasi-steady analysis. In summary, the dynamic load induced seal wear predicted by the gust simulation is reasonable.

A performance deterioration of a little over one percent was calculated for the once-per-airplane-life hard landing event. This flight condition is not considered pertinent to the deterioration problem and should only be viewed as the upper bound of performance loss which could result from extremely rare inertia loadings. The circumferential seal wear/rub map for the hard landing (Table XI) indicates rub depths

as high as 185 mils in the fan and 50 mils in the high-pressure turbine. Physically, interference of this magnitude results in a dynamic force on the rotor which inhibits or may even prevent further rotor blade to seal contact. The net result would be considerably less seal wear and change in TSFC than predicted by the analysis. Although an important consideration for highly dynamic events such as hard landings, modeling of the rotor to seal contact force was not economically feasible since a high degree of nonlinearity results. Consequently, the predicted results of seal wear and TSFC change for the hard landing simulation should be viewed only in a qualitative, not quantitative manner.

The seal wear/rub patterns resulting from the hard landing again indicate gyroscopic behavior to be responsible for much of the seal wear. The rub patterns for the hard landings are much more complex, however, as the inertia loads are sufficient to cause rub at the bottom of the case/seals and excite modes of the overhung components such as the low-pressure compressor and high-pressure turbine. A more detailed explanation of the seal wear pattern and rotor behavior for the landing events will be made for the revenue landing. Like the gust encounter, however, these causative factors and seal wear patterns appear to have a sound physical base.

The TSFC debit of about 0.2 percent predicted for the revenue landing was also higher than anticipated, consequently, a more detailed examination of the structural response to this condition was made. The rub map for the revenue landing (Table X) again shows the effects of gyroscopic type (side) motions and rubs. Inertia induced seal wear is also indicated for the low-pressure compressor and turbine stages. This result was somewhat surprising as the revenue landing sink rate of 3 ft/sec with a light fuel load would not be expected to produce inertia related seal wear.

As discussed in Section 6.3, the vertical displacement histories produced by the NASTRAN enforced dynamic displacement technique result in higher incremental inertia loadings than the displacement histories defined by the BCAC aeroelastic analysis. In addition to the increased inertia loadings, pitch rates from the aeroelastic analysis were also higher than anticipated. These two factors increase the gyroscopic behavior of the rotor and provide plausible reasons for the revenue service landing seal wear being higher than expected.

Additional insight into the rotor action and seal wear for the revenue landing may be gained by examining the modes of the structure which contribute significantly to the structural response. Since the mode shapes have been mass normalized, the generalized stiffness (Equation 16a) provides a relative measure of the energy of each mode while Equation 16b provides an absolute value of the energy stored in a given mode at any instant in time.

$$[\phi]^T [K][\phi] = [\omega^2] \qquad \text{Eqn. 16a}$$

$$[\eta]^T[\phi]^T [K][\phi][\eta] = E_m \qquad \text{Eqn. 16b}$$

Where E_m = modal elastic energy at a given instant of time.

The percent of the total elastic energy attributable to each mode of the analysis at each time point was tabulated for the revenue landing. The modes in which the majority of the system's elastic energy is contained are given in Table XIII. The time histories associated with the energy involvement of each of these modes are shown in Figure 41 through 45.

Although the freqencies of the participating modes are higher than anticipated, the sources of excitation for each mode in most cases is apparent. The strut lateral bending mode (No. 1) and horizontal fan case rocking mode (No. 16) are typically excited by gyroscopic action resulting from wing pitching and the excitation of modes with rotor bending. Modes with rotor bending (Nos. 10, 12) are typically excited by transient inertia loadings at touchdown. The engine torsion mode (No. 11) is more difficult to rationalize physically but may be excited by gyroscopic action in both the vertical and horizontal planes. Of particular interest is mode 12, which is primarily a low-pressure compressor case symmetric mode. The excitation of this mode may explain the more generalized seal wear occurring in the low-pressure compressor for the landing simulation.

SECTION 8.0

CONCLUSIONS

An analytical evaluation of the dynamic effects of three flight conditions of the JT9D-7/747 propulsion system has been conducted. Predicted performance changes associated with a once-per-flight vertical gust, typical revenue service landing, and a once-per-airframe life hard landing have been calculated. The analysis has provided valuable insight into the structural response of the JT9D-7 powerplant. With the exception of the once-per-life hard landing, the predicted dynamic load effects on TSFC were found to be negligibly small. These results strengthen the conclusions from the previous study (1) that steady aerodynamic pressure loads are probably responsible for the bulk of the TSFC loss predicted to be caused by flight loads. The results also indicate that the quasi-steady state approach to flight loads modeling is adequate to investigate the factors important to the deterioration process, especially the short-term aspect.

SECTION 9.0

REFERENCES

1 "Effect of Steady Flight Loads on JT9D-7 Performance Deterioration", A. Jay and E. S. Todd. NASA CR-135407, June 1978.

2. "Normal Modes Vibration Analysis of the JT9D/B747 Propulsion System", J. L. White and E. S. Todd, J. Aircraft, Vol. 15, No. 1, January 1978, pp. 28-32.

3 Analytical Methods in Vibrations, Leonard Meirovitch, The MacMillan Company, 1967, Chapter 9.

4 NASTRAN Theoretical Manual, Edited by Richard H. MacNeal, April 1972.

5 "Fast Modal Extraction in NASTRAN via the FEER Computer Program", Malcolm Newman and Aaron Pipano, NASA TM-X-2893, Sept. 1973.

6 "Coupling of Substructures for Dynamic Analysis", R. R Craig, Jr., and M. C. Bampton, AIAA J., Vol. 6, No. 7, July 1968, pp. 1313-1319.

7 MSC/NASTRAN Application Manual, Vol. 1, Section 2.4, The MacNeal-Schwendler Corporation.

TABLE I

STRUCTURAL MODEL SUMMARY

Substructure	Grid Points	Elements
Inlet Cowl	320	656
Fan and Low-Pressure Compressor	359	604
High-Pressure Compressor	464	516
Turbine	587	826
Tailcone	362	495
Wing Pylon	185	390
Rotors	171	513
Thrust Frame	5	4
	2453	4004

TABLE II

COWL FIXED BOUNDARY FREQUENCY SPECTRUM
(Frequencies in Hertz)

Symmetric		Antisymmetric	
20.73	1436.84	14.75	1741.61
57.60	1482.10	169.51	1776.02
114.05	1494.50	275.84	1915.32
166.64	1550.27	288.05	2021.95
266.14	1560.19	372.62	2129.97
304.14	1635.95	423.27	2143.02
363.13	1649.09	450.76	2185.00
371.13	1758.25	468.94	
456.12	1910.88	496.96	
481.47	2018.04	511.44	
498.00	2040.94	527.57	
507.97	2128.87	543.25	
518.39	2148.81	555.58	
543.23	2184.35	569.16	
560.33	2270.35	622.51	
571.33	2429.67	626.16	
574.55	2632.26	670.36	
597.97		691.30	
613.85		783.50	
634.14		786.80	
638.15		828.65	
639.11		873.47	
656.27		903.05	
696.37		1020.83	
728.66		1037.65	
764.69		1157.57	
864.42		1175.59	
871.61		1195.84	
911.26		1285.32	
935.22		1295.64	
970.45		1301.69	
987.18		1336.78	
1094.00		1343.82	
1164.26		1366.25	
1206.26		1545.02	
1238.74		1565.99	
1302.46		1597.67	
1330.65		1640.61	
1360.57		1727.54	

TABLE III

FAN FIXED BOUNDARY FREQUENCY SPECTRUM
(Frequencies in Hertz)

Symmetric		Antisymmetric	
95.05	330.68	93.88	352.36
103.15	332.89	100.49	355.48
126.73	338.26	126.77	357.05
134.17	353.39	137.61	358.58
161.13	353.99	159.75	369.99
175.98	358.98	176.12	372.08
176.44	362.18	177.50	386.34
178.48	369.97	178.33	402.78
183.08	375.59	181.68	404.00
185.77	393.73	184.12	407.22
186.40	402.79	185.62	411.34
187.77	404.02	187.97	423.87
189.52	407.55	189.69	430.99
189.91	407.74	190.83	436.36
191.46	409.74	204.03	438.47
204.60	414.32	204.94	439.92
204.92	420.05	205.13	447.96
205.92	429.89	208.17	453.66
208.80	430.32	233.46	462.57
220.78	434.85	241.68	462.95
233.47	436.38	241.95	468.24
241.83	439.21	244.01	484.34
242.61	439.93	245.59	485.79
244.96	445.65	246.71	494.66
247.22	448.20	263.19	498.00
249.14	456.45	267.78	502.42
265.53	461.81	271.40	506.83
268.36	462.81	273.62	523.56
272.88	463.19	275.92	530.78
273.25	464.62	278.71	532.57
276.53	471.38	278.97	537.79
277.56	480.59	280.39	539.86
280.88	484.53	289.19	541.13
281.34		289.29	
281.78		294.19	
289.14		301.37	
290.05		311.63	
294.17		316.82	
309.18		330.70	
313.94		332.15	
316.03		337.34	
320.31		338.69	

TABLE IV

HPC FIXED BOUNDARY FREQUENCY SPECTRUM
(Frequencies in Hertz)

Symmetric		Antisymmetric	
126.70	669.95	157.09	712.57
163.50	671.89	174.38	730.60
194.04	682.51	216.02	737.95
214.47	699.42	234.63	745.09
250.75	703.77	253.45	750.58
282.73	720.45	307.98	752.61
300.42		314.16	
306.59		335.83	
331.18		347.58	
336.41		384.96	
360.08		388.35	
373.57		411.36	
384.78		432.36	
398.05		437.57	
415.76		472.70	
436.41		473.17	
453.39		478.62	
478.81		487.86	
481.73		497.28	
491.67		499.10	
502.01		505.12	
517.70		515.33	
521.05		518.44	
528.27		525.49	
529.53		547.20	
543.99		556.35	
546.40		563.38	
557.15		570.43	
563.84		579.89	
568.42		586.89	
577.70		590.46	
580.53		592.29	
583.95		595.89	
589.05		603.78	
594.44		607.06	
598.03		610.05	
608.34		632.22	
608.67		640.73	
615.52		672.19	
618.22		679.36	
633.61		692.69	
638.55		697.43	
652.30		706.27	

TABLE V

TURBINE FIXED BOUNDARY FREQUENCY SPECTRUM
(Frequencies in Hertz)

Symmetric			Antisymmetric		
35.87	457.10	616.96	43.69	464.57	677.55
47.96	463.79	621.02	77.11	473.92	677.99
76.12	465.34	640.82	88.13	477.92	679.89
86.64	477.02	646.20	98.10	485.10	684.26
107.65	480.14	648.08	108.58	487.20	694.46
119.29	483.89	653.23	120.25	490.60	703.39
126.68	484.36	669.54	128.80	491.88	709.40
128.99	488.83	672.32	128.99	492.90	713.51
129.38	490.73	676.79	129.05	499.18	739.60
133.55	491.69	677.92	134.17	499.81	743.45
134.51	493.72	679.69	134.93	505.75	744.17
140.22	494.37	680.42	141.06	508.27	751.93
142.91	499.27	697.16	143.33	512.84	762.78
143.34	501.11	709.71	150.28	516.17	775.90
153.71	508.22		153.90	521.60	
162.36	510.68		162.55	523.27	
165.85	512.02		195.63	528.24	
192.31	516.05		216.21	529.24	
207.90	520.32		223.57	535.85	
215.75	523.60		231.99	545.42	
223.67	528.60		243.06	545.98	
242.76	535.91		250.24	548.33	
249.96	540.66		256.95	550.62	
257.07	543.37		267.72	560.02	
264.72	545.63		278.22	568.85	
267.88	546.07		282.62	573.25	
277.17	548.99		293.41	577.88	
284.01	550.95		305.52	581.08	
301.61	552.28		309.12	586.21	
306.29	564.53		316.02	593.25	
309.68	569.34		350.19	593.47	
349.90	573.33		350.36	593.73	
361.15	578.06		362.60	595.95	
363.55	592.01		363.80	598.92	
364.70	593.53		365.67	600.38	
367.85	594.54		366.43	606.05	
386.56	598.74		389.84	606.46	
388.47	599.31		390.81	610.26	
391.75	600.99		418.62	642.34	
401.74	601.29		426.50	644.09	
417.93	605.14		428.87	659.91	
428.77	605.67		454.85	669.31	
432.25	607.34		462.70	674.67	

TABLE VI

TAILCONE-FIXED BOUNDARY FREQUENCY SPECTRUM
(Frequencies in Hertz)

Symmetric		Antisymmetric	
85.12	2886.15	85.07	
222.55	3186.83	226.68	3612.79
329.67	3275.93	328.81	3932.11
367.02	3436.48	336.62	4316.98
373.20	3492.84	369.78	4413.85
392.37	3933.30	376.43	4707.55
569.44	4259.05	575.93	4943.55
688.15	5322.21	687.39	5424.05
721.65		721.43	6576.91
882.33		917.70	
907.50		985.36	
951.22		100.33	
990.76		1100.39	
1099.93		1158.61	
1152.42		1192.38	
1267.76		1277.04	
1279.99		1285.96	
1317.25		1324.47	
1337.23		1346.05	
1355.81		1362.88	
1377.19		1379.53	
1404.96		1418.33	
1436.15		1461.22	
1451.07		1467.13	
1471.91		1477.60	
1488.16		1502.00	
1496.44		1513.83	
1526.41		1529.02	
1539.25		1920.27	
1625.22		1930.52	
1783.56		1975.27	
1921.58		2049.29	
2023.64		2196.42	
2136.77		2248.12	
2202.30		2272.99	
2236.37		2403.52	
2402.99		2878.56	
2466.19		2942.61	
2531.69		2947.40	
2786.60		3126.25	
2828.89		3304.45	
2873.65		3433.23	

TABLE VII

STRUT FIXED BOUNDARY FREQUENCY SPECTRUM
(Frequencies in Hertz)

Symmetric	Antisymmetric
121.23	59.83
177.08	95.05
193.97	102.32
213.89	110.33
238.77	165.08
275.18	195.60
293.68	226.86
324.66	235.24
390.70	256.75
410.01	294.00
425.97	334.33
471.77	346.56
479.42	357.58
488.89	372.15
519.56	415.06
522.49	459.67
530.01	477.75
559.24	482.57
564.69	507.07
580.98	528.41
586.36	538.81
670.53	560.88
673.36	629.13
696.91	659.99
742.24	664.71
773.76	679.37
832.49	
856.44	

TABLE VIII

INTEGRATED PROPULSION SYSTEM FREQUENCIES

Mode	S or A *	Frequency (Hz)	Test Results (Hz)	Description
1	A	2.5199	2.4	First Pylon Lateral
2	S	4.4986	4.6	First Pylon Vertical
3	A	6.8272	6.5	Strut Torsion
4	S	11.115		Thrust (Y) Frame, Engine Axial
5	A	12.836		Engine Roll
6	A	14.497		Fan Case Rocking - Side
7	S	14.816		Fan Case Rocking - Vertical
8	A	19.123		
9	S	20.089		Fan Thrust Reversers
10	S	24.510		Higher Pylon Bending With Low Rotor Motion
11	A	27.489		Case Torsion, Low Rotor Bending
12	S	29.024		
13	S	31.809		
14	A	32.499		
15	S	35.126		
16	A	37.833		Core Engine Bending
17	S	45.539		
18	A	45.556		
19	S	46.648		
20	A	51.473		
21	S	53.351		
22	A	54.059		
23	S	56.636	56.	Tailcone Wagging, Low Rotor Bending
24	S	62.207		
25	A	63.216		
26	S	70.002		
27	S	70.896		
28	A	72.600		
29	S	74.723		
30	A	75.101		
31	A	75.865		
32	A	76.513		
33	S	77.930		
34	A	83.489		
35	S	86.212		
36	S	87.184		
37	A	87.775		
38	A	88.225		
39	S	89.475		
40	A	90.955		

* S = symmetric mode
A = antisymmetric mode

TABLE VIII (Cont'd)

INTEGRATED PROPULSION SYSTEM FREQUENCIES

Mode	S or A *	Frequency (Hz)	Test Results (Hz)	Description
41	S	93.189		
42	A	93.732		
43	S	94.828		
44	A	95.689		
45	A	97.376		
46	A	98.838		
47	S	99.287		
48	A	101.64		
49	S	102.75		
50	A	103.75		
51	S	104.26		
52	A	106.65		
53	S	107.65		
54	S	107.79		
55	A	108.57		
56	S	114.22		
57	A	115.61		
58	S	116.06		
59	S	118.03		
60	A	118.14		
61	S	119.31		
62	A	120.27		
63	A	120.35		
64	A	122.94		
65	S	125.73		
66	S	126.28		
67	A	126.77		
68	S	126.80		
69	S	126.90		
70	S	127.67		
71	A	128.80		
72	A	128.98		
73	A	128.99		
74	S	129.02		
75	A	129.04		
76	S	129.41		
77	A	130.71		
78	A	132.54		
79	S	133.57		
80	A	134.17		

* S = symmetric mode
A = antisymmetric mode

TABLE VIII (Cont'd)

INTEGRATED PROPULSION SYSTEM FREQUENCIES

Mode	S or A *	Frequency (Hz)	Test Results (Hz)	Description
81	S	134.52		
82	A	134.91		
83	A	136.26		
84	S	136.97		
85	S	140.20		
86	A	141.06		
87	S	143.04		
88	S	143.20		
89	A	143.33		
90	A	147.27		
91	A	151.59		
92	S	152.25		
93	S	153.71		
94	A	153.90		
95	S	154.58		
96	A	159.33		
97	S	159.49		
98	A	159.72		
99	S	161.03		
100	A	162.55		

* S = symmetric mode
A = antisymmetric mode

TABLE IX

CIRCUMFERENTIAL RUB PATTERN FOR
ONCE-PER-FLIGHT VERTICAL GUST
(Rub Depths in mils)

Engine Stages

DEGREES *	FAN	2 LPC	3 LPC	4 LPC	5 HPC	6 HPC	7 HPC	8 HPC	9 HPC	10 HPC	11 HPC	12 HPC	13 HPC	14 HPC	15 HPC	1 HPT	2 HPT	3 LPT	4 LPT	5 LPT	6 LPT
0.	0.	0.	0.	0.	0.	0.	0.	0.	0.	0.	0.	0.	0.	0.	0.	0.	0.	0.	0.	0.	0.
12.	0.	0.	0.	0.	0.	0.	0.	0.	0.	0.	0.	0.	0.	0.	0.	0.	0.	0.	0.	0.	0.
24.	0.	0.	0.	0.	0.	0.	0.	0.	0.	0.	0.	0.	0.	0.	0.	0.	0.	0.	0.	0.	0.
36.	3.	0.	0.	0.	0.	0.	0.	0.	0.	0.	0.	0.	0.	0.	0.	0.	0.	0.	0.	0.	0.
48.	9.	0.	0.	1.	0.	0.	0.	0.	0.	0.	0.	0.	0.	0.	0.	0.	0.	0.	0.	0.	0.
60.	15.	0.	0.	3.	0.	0.	0.	0.	0.	0.	0.	0.	0.	0.	0.	0.	0.	0.	0.	0.	0.
72.	25.	0.	0.	5.	0.	0.	0.	0.	0.	0.	0.	0.	0.	0.	0.	0.	0.	0.	0.	0.	0.
84.	38.	0.	0.	6.	0.	0.	0.	0.	0.	0.	0.	0.	0.	0.	0.	0.	0.	0.	0.	0.	0.
96.	43.	0.	0.	4.	0.	0.	0.	0.	0.	0.	0.	0.	0.	0.	0.	0.	0.	0.	0.	0.	0.
108.	35.	0.	0.	0.	0.	0.	0.	0.	0.	0.	0.	0.	0.	0.	0.	0.	0.	0.	0.	0.	0.
120.	19.	0.	0.	0.	0.	0.	0.	0.	0.	0.	0.	0.	0.	0.	0.	0.	0.	0.	0.	0.	0.
132.	4.	0.	0.	0.	0.	0.	0.	0.	0.	0.	0.	0.	0.	0.	0.	0.	0.	0.	0.	0.	0.
144.	0.	0.	0.	0.	0.	0.	0.	0.	0.	0.	0.	0.	0.	0.	0.	0.	0.	0.	0.	0.	0.
156.	0.	0.	0.	0.	0.	0.	0.	0.	0.	0.	0.	0.	0.	0.	0.	0.	0.	0.	0.	0.	0.
168.	0.	0.	0.	0.	0.	0.	0.	0.	0.	0.	0.	0.	0.	0.	0.	0.	0.	0.	0.	0.	0.
180.	0.	0.	0.	0.	0.	0.	0.	0.	0.	0.	0.	0.	0.	0.	0.	0.	0.	0.	0.	0.	0.
192.	0.	0.	0.	0.	0.	0.	0.	0.	0.	0.	0.	0.	0.	0.	0.	0.	0.	0.	0.	0.	0.
204.	0.	0.	0.	0.	0.	0.	0.	0.	0.	0.	0.	0.	0.	0.	0.	0.	0.	0.	0.	0.	0.
216.	0.	0.	0.	0.	0.	0.	0.	0.	0.	0.	0.	0.	0.	0.	0.	0.	0.	0.	0.	0.	0.
228.	0.	0.	0.	0.	0.	0.	0.	0.	0.	0.	0.	0.	0.	0.	0.	0.	0.	0.	0.	0.	0.
240.	0.	0.	0.	0.	0.	0.	0.	0.	0.	0.	0.	0.	0.	0.	0.	0.	0.	0.	0.	0.	0.
252.	0.	0.	0.	0.	0.	0.	0.	0.	0.	0.	0.	0.	0.	0.	0.	0.	0.	0.	0.	0.	0.
264.	7.	0.	0.	10.	0.	0.	0.	0.	0.	0.	0.	0.	0.	0.	0.	0.	0.	0.	0.	0.	0.
276.	10.	0.	0.	19.	0.	0.	0.	0.	0.	0.	0.	0.	0.	0.	0.	0.	0.	0.	0.	0.	0.
288.	6.	0.	0.	20.	0.	0.	0.	0.	0.	0.	0.	0.	0.	0.	0.	0.	0.	0.	0.	0.	0.
300.	3.	0.	0.	17.	0.	0.	0.	0.	0.	0.	0.	0.	0.	0.	0.	0.	0.	0.	0.	0.	0.
312.	1.	0.	0.	11.	0.	0.	0.	0.	0.	0.	0.	0.	0.	0.	0.	0.	0.	0.	0.	0.	0.
324.	0.	0.	0.	4.	0.	0.	0.	0.	0.	0.	0.	0.	0.	0.	0.	0.	0.	0.	0.	0.	0.
336.	0.	0.	0.	0.	0.	0.	0.	0.	0.	0.	0.	0.	0.	0.	0.	0.	0.	0.	0.	0.	0.
348.	0.	0.	0.	0.	0.	0.	0.	0.	0.	0.	0.	0.	0.	0.	0.	0.	0.	0.	0.	0.	0.

*Circumferential location in degrees, viewed (clockwise) from front of the engine; 0 degrees is at top of the engine.

TABLE X

CIRCUMFERENTIAL RUB PATTERN FOR
REVENUE SERVICE LANDING SIMULATION
(Rub Depths in mils)

Engine Stages

DEGREES *	FAN	2 LPC	3 LPC	4 LPC	5 HPC	6 HPC	7 HPC	8 HPC	9 HPC	10 HPC	11 HPC	12 HPC	13 HPC	14 HPC	15 HPC	1 HPT	2 HPT	3 LPT	4 LPT	5 LPT	6 LPT
0.	0.	0.	0.	0.	0.	0.	0.	0.	0.	0.	0.	0.	0.	0.	0.	0.	0.	5.	0.	0.	0.
12.	0.	0.	0.	0.	0.	0.	0.	0.	0.	0.	0.	0.	0.	0.	0.	0.	0.	4.	0.	0.	0.
24.	0.	0.	0.	0.	0.	0.	0.	0.	0.	0.	0.	0.	0.	0.	0.	0.	0.	1.	0.	0.	0.
36.	0.	0.	0.	3.	0.	0.	0.	0.	0.	0.	0.	0.	0.	0.	0.	0.	0.	0.	0.	0.	0.
48.	0.	0.	0.	11.	0.	0.	0.	0.	0.	0.	0.	0.	0.	0.	0.	0.	0.	0.	0.	0.	0.
60.	0.	0.	0.	24.	0.	0.	0.	0.	0.	0.	0.	0.	0.	0.	0.	0.	0.	12.	0.	0.	0.
72.	0.	0.	0.	36.	0.	0.	0.	0.	0.	0.	0.	0.	0.	0.	0.	0.	4.	27.	2.	0.	0.
84.	2.	0.	0.	43.	0.	0.	0.	0.	0.	0.	0.	0.	0.	0.	0.	0.	5.	37.	9.	0.	0.
96.	10.	0.	0.	36.	0.	0.	0.	0.	0.	0.	0.	0.	0.	0.	0.	0.	3.	39.	11.	0.	0.
108.	15.	0.	0.	21.	0.	0.	0.	0.	0.	0.	0.	0.	0.	0.	0.	0.	0.	33.	6.	0.	0.
120.	0.	0.	0.	6.	0.	0.	0.	0.	0.	0.	0.	0.	0.	0.	0.	0.	0.	23.	0.	0.	0.
132.	0.	0.	0.	1.	0.	0.	0.	0.	0.	0.	0.	0.	0.	0.	0.	0.	0.	10.	0.	0.	0.
144.	0.	0.	3.	4.	0.	0.	0.	0.	0.	0.	0.	0.	0.	0.	0.	0.	0.	0.	0.	0.	0.
156.	0.	0.	6.	12.	0.	0.	0.	0.	0.	0.	0.	0.	0.	0.	0.	0.	0.	0.	0.	0.	0.
168.	0.	0.	9.	21.	0.	0.	0.	0.	0.	0.	0.	0.	0.	0.	0.	0.	0.	0.	0.	0.	0.
180.	0.	0.	10.	21.	0.	0.	0.	0.	0.	0.	0.	0.	0.	0.	0.	0.	0.	7.	3.	0.	0.
192.	0.	0.	10.	20.	0.	0.	0.	0.	0.	0.	0.	0.	0.	0.	0.	0.	0.	15.	0.	0.	0.
204.	0.	0.	5.	15.	0.	0.	0.	0.	0.	0.	0.	0.	0.	0.	0.	0.	0.	19.	0.	0.	0.
216.	0.	0.	1.	8.	0.	0.	0.	0.	0.	0.	0.	0.	0.	0.	0.	0.	0.	20	0.	0.	0.
228.	0.	0.	0.	2.	0.	0.	0.	0.	0.	0.	0.	0.	0.	0.	0.	0.	0.	19.	0.	0.	0.
240.	0.	0.	0.	0.	0.	0.	0.	0.	0.	0.	0.	0.	0.	0.	0.	0.	0.	16.	0.	0.	0.
252.	10.	0.	0.	0.	0.	0.	0.	0.	0.	0.	0.	0.	0.	0.	0.	0.	0.	12.	0.	0.	0.
264.	14.	0.	0.	9.	0.	0.	0.	0.	0.	0.	0.	0.	0.	0.	0.	0.	0.	11.	0.	0.	0.
276.	16.	0.	0.	17.	0.	0.	0.	0.	0.	0.	0.	0.	0.	0.	0.	0.	0.	10.	0.	0.	0.
288.	19.	0.	0.	18.	0.	0.	0.	0.	0.	0.	0.	0.	0.	0.	0.	0.	0.	6.	0.	0.	0.
300.	18.	0.	0.	16.	0.	0.	0.	0.	0.	0.	0.	0.	0.	0.	0.	0.	0.	6.	0.	0.	0.
312.	4.	0.	0.	15.	0.	0.	0.	0.	0.	0.	0.	0.	0.	0.	0.	0.	0.	0.	0.	0.	0.
324.	0.	0.	0.	6.	0.	0.	0.	0.	0.	0.	0.	0.	0.	0.	0.	0.	0.	0.	0.	0.	0.
336.	0.	0.	0.	0.	0.	0.	0.	0.	0.	0.	0.	0.	0.	0.	0.	0.	0.	1.	0.	0.	0.
348.	0.	0.	0.	0.	0.	0.	0.	0.	0.	0.	0.	0.	0.	0.	0.	0.	0.	4.	0.	0.	0.

*Circumferential location in degrees, viewed (clockwise) from front of the engine; 0 degrees is at top of the engine.

TABLE XI

CIRCUMFERENTIAL RUB PATTERN FOR
HARD LANDING SIMULATION
(Rub Depths in mils)

Engine Stages

DEGREES *	FAN	2 LPC	3 LPC	4 LPC	5 HPC	6 HPC	7 HPC	8 HPC	9 HPC	10 HPC	11 HPC	12 HPC	13 HPC	14 HPC	15 HPC	1 HPT	2 HPT	3 LPT	4 LPT	5 LPT	6 LPT
0.	0.	0.	0.	0.	0.	0.	0.	0.	0.	0.	0.	0.	0.	0.	0.	0.	0.	0.	0.	0.	0.
12.	0.	0.	0.	0.	0.	0.	0.	0.	0.	0.	0.	0.	0.	0.	0.	0.	0.	0.	0.	0.	0.
24.	0.	0.	0.	0.	0.	0.	0.	0.	0.	0.	0.	0.	0.	0.	0.	0.	1.	0.	0.	0.	0.
36.	0.	0.	0.	12.	0.	0.	0.	0.	0.	0.	0.	0.	0.	0.	0.	0.	15.	1.	0.	0.	0.
48.	0.	0.	0.	38.	0.	0.	0.	0.	0.	0.	0.	0.	0.	0.	0.	5.	27.	14.	0.	0.	0.
60.	0.	0.	1.	69.	0.	0.	0.	0.	0.	0.	0.	0.	0.	0.	0.	15.	39.	31.	7.	0.	0.
72.	18.	0.	10.	86.	0.	0.	0.	0.		0.	0.	0.	0.	0.	0.	22.	48.	53.	21.	0.	0.
84.	72.	0.	19.	88.	0.	0.	0.	0.		0.	0.	0.	0.	0.	0.	21.	48.	67.	28.	0.	0.
96.	138.	4.	21.	78.	0.	0.	0.	0.	0.	0.	0.	0.	0.	0.	0	15.	42.	67.	29.	0.	0.
108.	185.	14.	17.	61.	0.	0.	0.	0.	0.	0.	0.	0.	0.	0.	0.	5.	31.	55.	22.	0.	0.
120.	181.	30.	15.	45.	0.	0.	0.	0.	0.	0.	0.	0.	0.	0.	0.	0.	15.	37.	8.	0.	0.
132.	136.	41.	27.	39.	0.	0.	0.	0.	0.	0.	0.	0.	0.	0.	0.	0.	0.	19.	0.	0.	0.
144.	77.	46.	45.	42.	0.	0.	0.	0.	0.	0.	0.	0.	0.	0.	0.	0.	0.	5.	0.	0.	0.
156.	27.	43.	58.	50.	0.	0.	0.	0.	0.	0.	0.	0.	0.	0.	0.	0.	0.	0.	0.	0.	0.
168.	0.	35.	64.	58.	0.	0.	0.	0.	0.	0.	0.	0.	0.	0.	0.	0.	0.	0.	0.	0.	0.
180.	0.	20.	63.	60.	0.	0.	0.	0.	0.	0.	0.	0.	0.	0.	0.	0.	0.	0.	0.	0.	0.
192.	0.	37.	62.	57.	0.	0	0.	0.	0.	0.	0.	0.	0.	0.	0.	0.	0.	0.	0.	0.	0.
204.	19.	47.	53.	47.	0.	0.	0.	0.	0.	0.	0.	0.	0.	0.	0.	0.	0.	0.	0.	0.	0.
216.	49.	50.	35.	38.	0.	0.	0.	0.	0.	0.	0.	0.	0.	0.	0.	0.	0.	12.	0.	0.	0.
228.	77.	47.	14.	33.	0.	0.	0.	0.	0.	0.	0.	0.	0.	0.	0.	0.	11.	31.	5.	0.	0.
240.	92.	37.	0.	32.	0.	0.	0.	0.	0.	0.	0.	0.	0.	0.	0.	14.	26.	51.	22.	0.	0.
252.	80.	16.	5.	45.	0.	0.	0.	0.	0.	0.	0.	0.	0.	0.	0.	26.	39.	70.	36.	0.	0.
264.	43.	4.	11.	70.	0.	0.	0.	0.	0.	0.	0.	0.	0.	0.	0.	31.	47.	80.	44.	0.	0.
276.	13.	0.	17.	87.	0.	0.	0.	0.	0.	0.	0.	0.	0.	0.	0.	29.	50.	80.	44.	0.	0.
288.	0.	0.	19.	86.	0.	0.	0.	0.	0.	0.	0.	0.	0.	0.	0.	22.	49.	68.	36.	0.	0.
300.	0.	0.	16.	74.	0.	0.	0.	0.	0.	0.	0.	0.	0.	0.	0.	11.	35.	49.	20.	0.	0.
312.	0.	0.	7.	53.	0.	0.	0.	0.	0.	0.	0.	0.	0.	0.	0.	0.	19.	30.	3.	0.	0.
324.	0.	0.	2.	19.	0.	0.	0.	0.	0.	0.	0.	0.	0.	0.	0.	0.	3.	15.	0.	0.	0.
336.	0.	0.	0.	0.	0.	0.	0.	0.	0.	0.	0.	0.	0.	0.	0.	0.	0.	0.	0.	0.	0.
348.	0.	0.	0.	0.	0.	0.	0.	0.	0.	0.	0.	0.	0.	0.	0.	0.	0.	0.	0.	0.	0.

*Circumferential location in degrees, viewed (clockwise) from front of the engine; 0 degrees is at top of the engine.

TABLE XII

CALIBRATION OF COMPUTED FREQUENCY SPECTRUM

	NASTRAN Analysis (Hertz)	Test(T) or Analysis(A) (Hertz)
Strut Lateral Bending	2.52	2.40(T)
Strut Vertical Bending	4.50	4.60(T)
Strut Torsion	6.50	6.80(T)
Tailcone Vertical Wagging	56.60	56.00(T)
Fan Case Rocking/Low Rotor	24.51	22.83(A)
LPC Case Bending/Low Rotor	29.02	30.17(A)

TABLE XIII

HIGH ENERGY MODES FOR TYPICAL REVENUE SERVICE LANDING

Mode No.	Frequency (Hertz)	General Description
1	2.51	Strut Lateral Bending
10	24.51	Vertical Fan Rocking, Low-Pressure Spool Rotor Bending
11	27.49	Engine Torsion, Low-Pressure Spool Rotor Bending
12	29.02	Low-Pressure Compressor Case Vertical Bending, Low-Pressure Spool Rotor Bending
16	37.833	Core Engine Bending, Lateral Fan Case Rocking

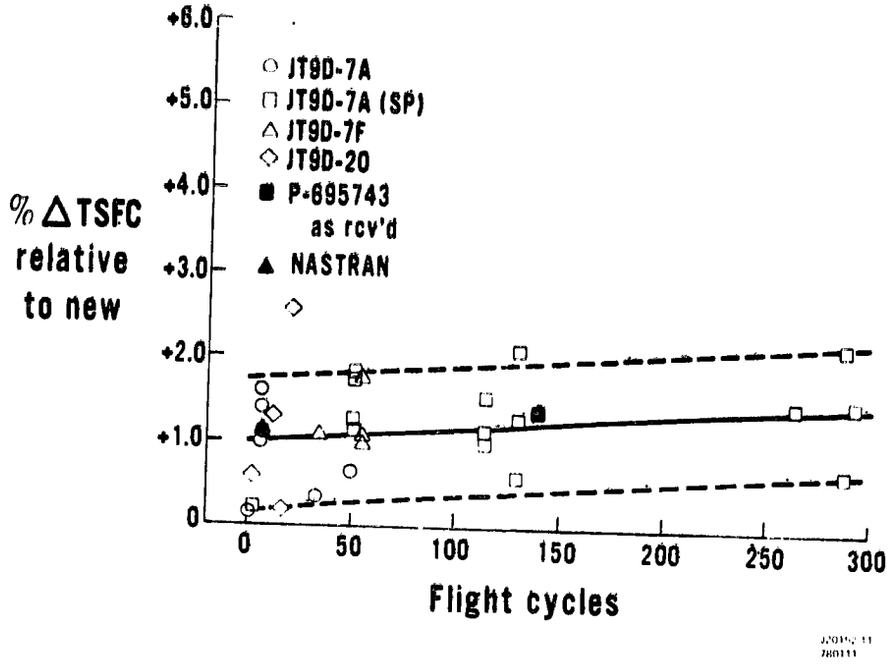

Figure 1 Comparison of Predicted Performance Deterioration Based on Analysis of Steady Flight Loads with Fleet Performance Data

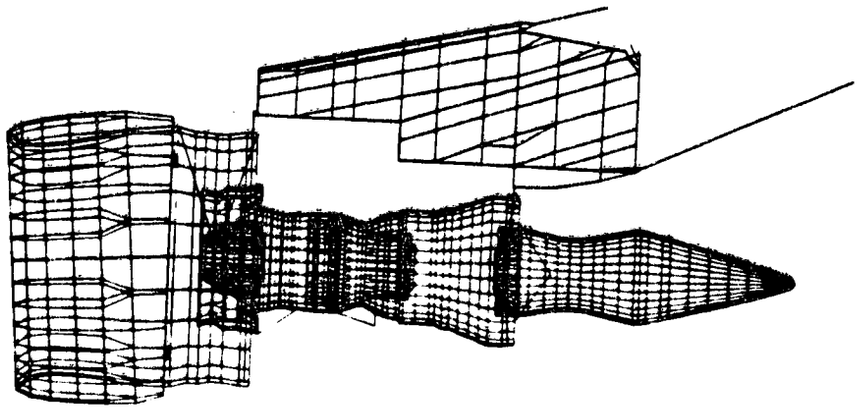

Figure 2 JT9D-7/747 Integrated NASTRAN Finite Element Structural Model

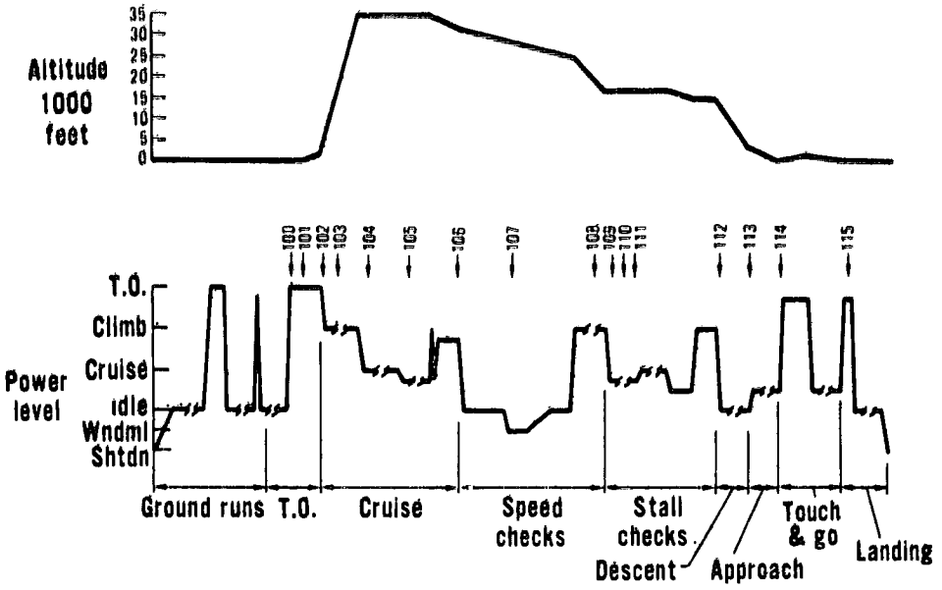

Figure 3 Typical Flight Profile Analyzed in the Steady Loads Analysis

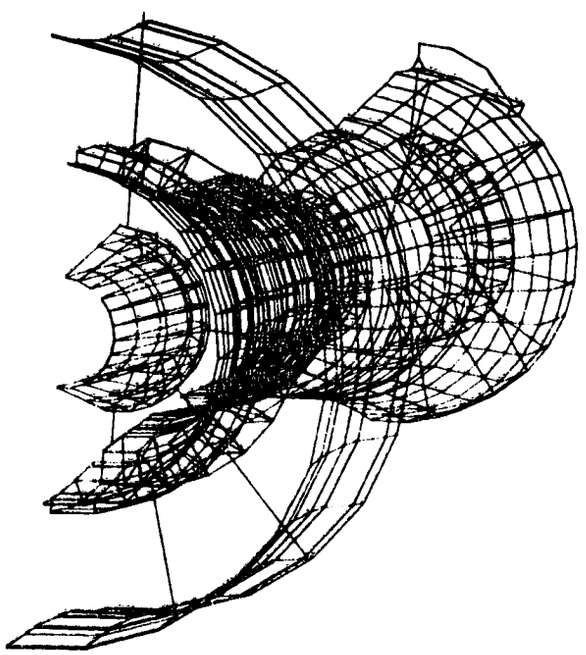

Figure 4 JT9D-7 Finite Element Model Displaying Use of Structural Symmetry

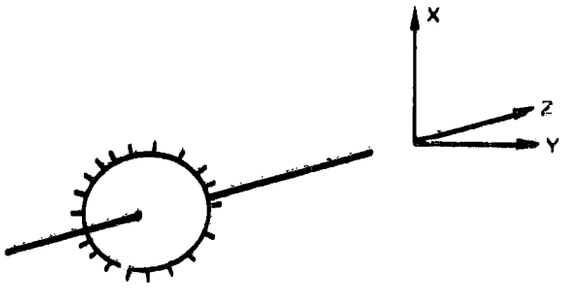

Figure 5 Orientation of a Typical Rotor Stage to the Analysis Coordinate System

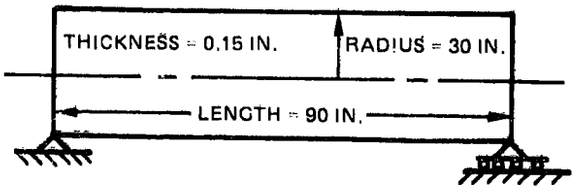

Figure 6 Simply Supported Cylindrical Shell Used in Evaluation of Dynamic Reduction Procedures

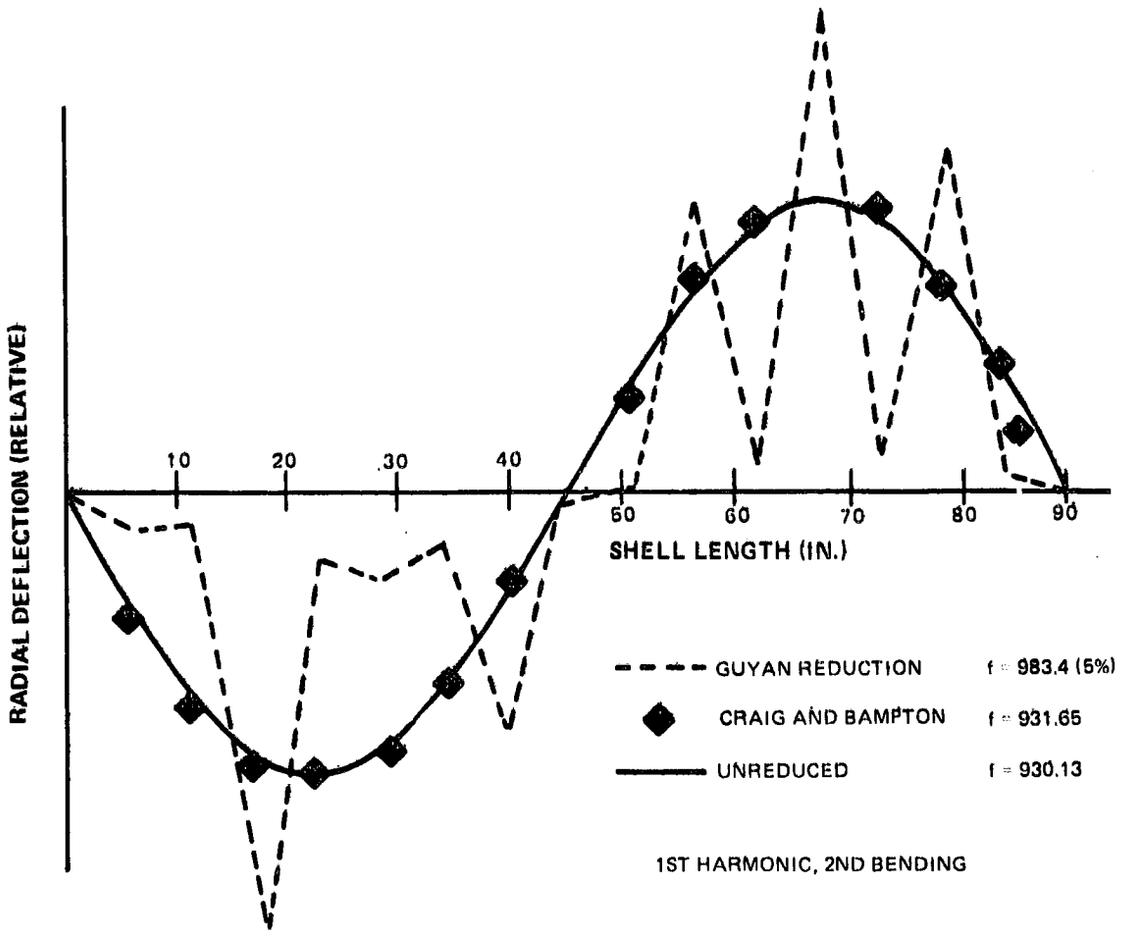

Figure 7 Mode Shape Comparisons for Simply Supported Cylindrical Shell of Figure 6

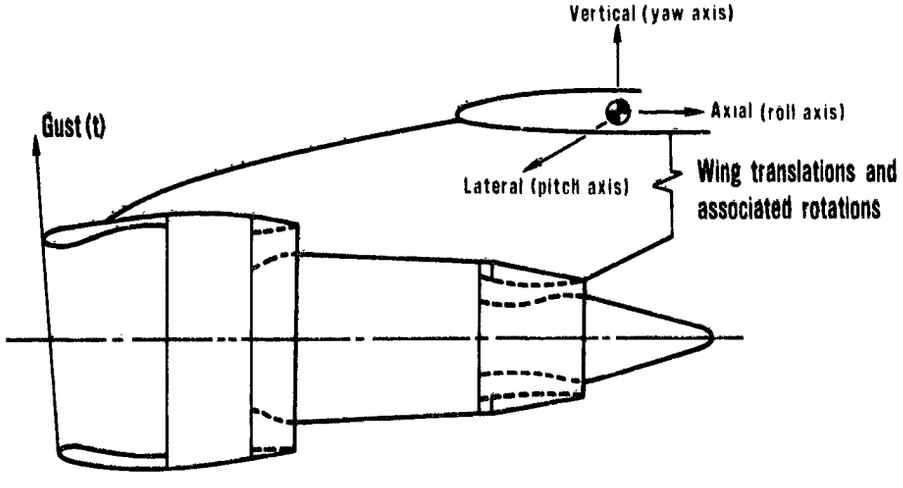

Figure 8 Wing Displacement Coordinate System

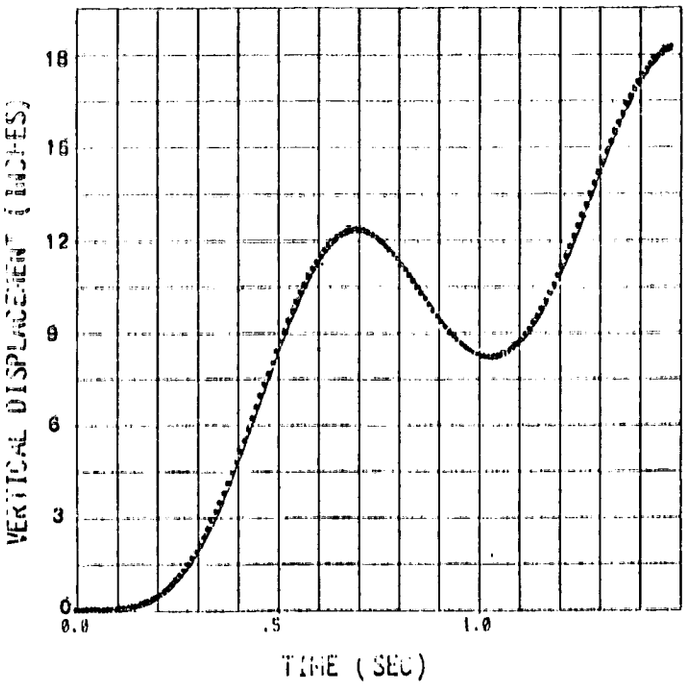

Figure 9 Wing Vertical Displacement History for Once-Per-Flight Vertical Gust

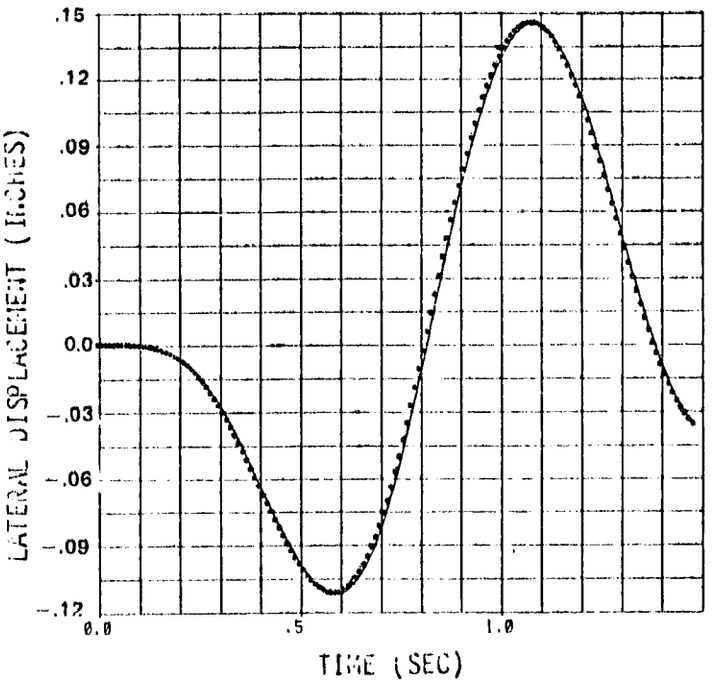

Figure 10 Wing Lateral Displacement History for Once-Per-Flight Vertical Gust

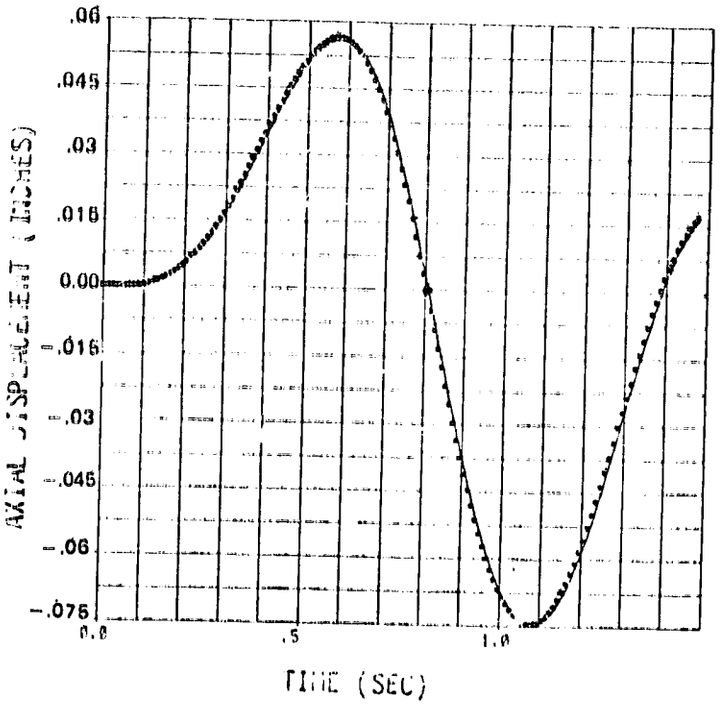

Figure 11 Wing Longitudinal Displacement History for Once-Per-Flight Vertical Gust

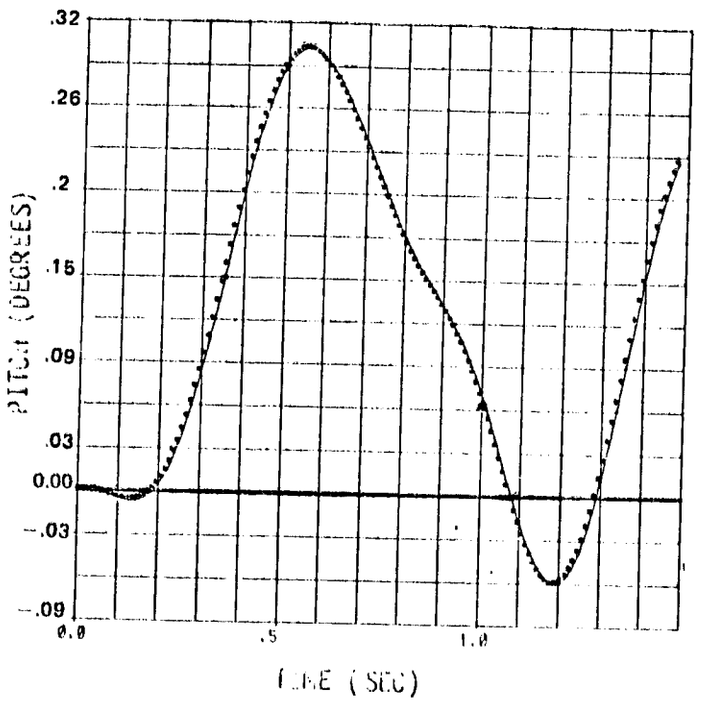

Figure 12 Wing Pitch History for Once-Per-Flight Vertical Gust

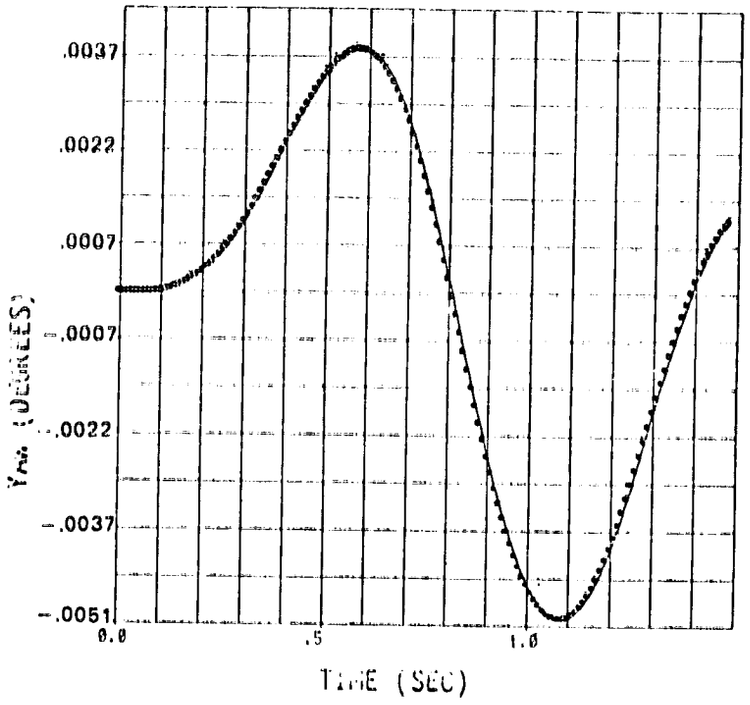

Figure 13 Wing Yaw History for Once-Per-Flight Vertical Gust

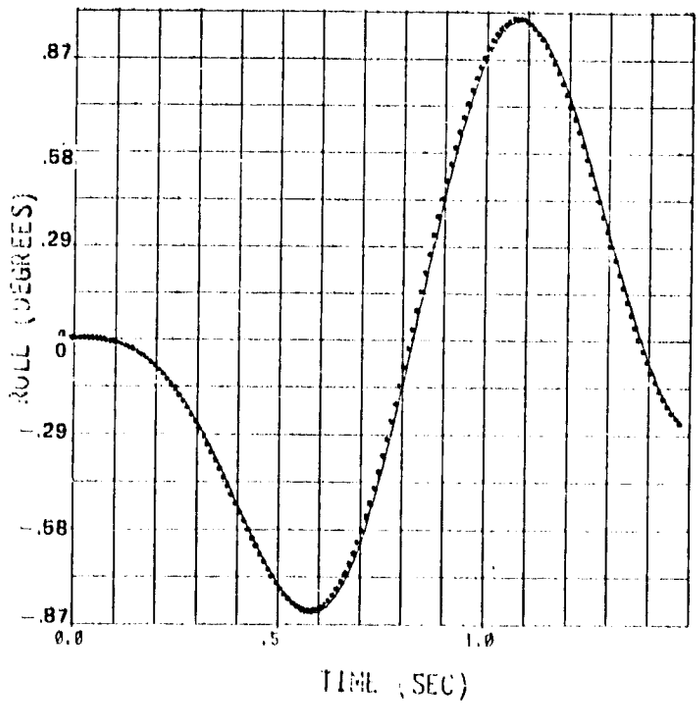

Figure 14 Wing Roll History for Once-Per-Flight Vertical Gust

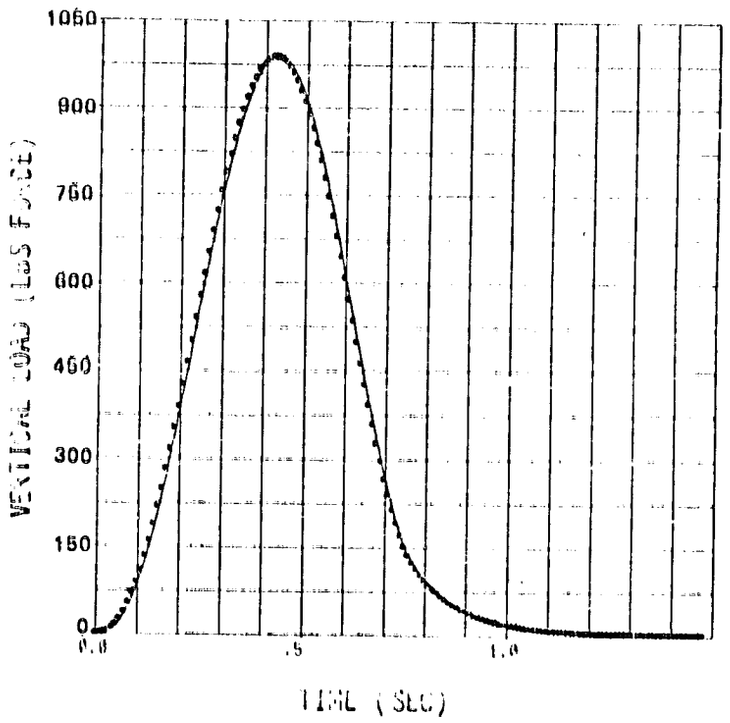

Figure 15 Cowl Incremental Vertical Load History for Once-Per-Flight Vertical Gust

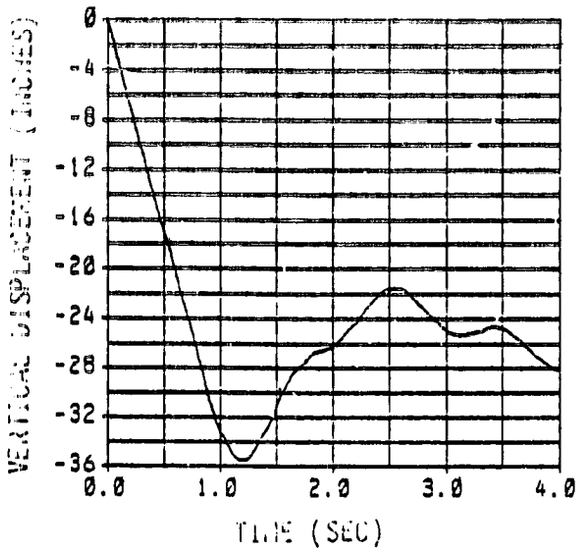

Figure 16 Wing Vertical Displacement History for Typical Revenue Service Landing

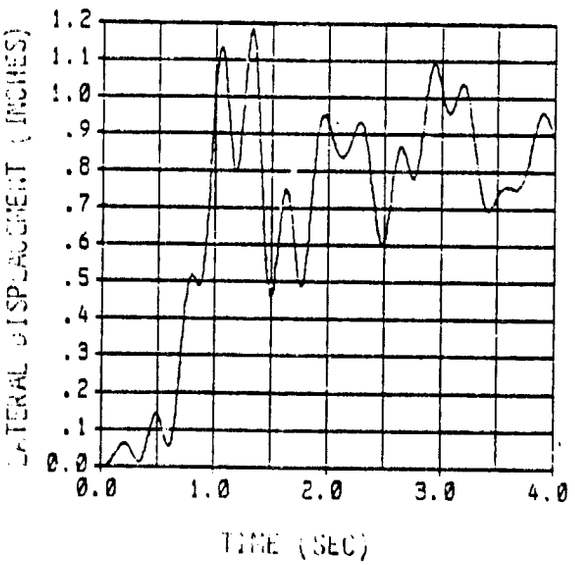

Figure 17 Wing Lateral Displacement History for Typical Revenue Service Landing

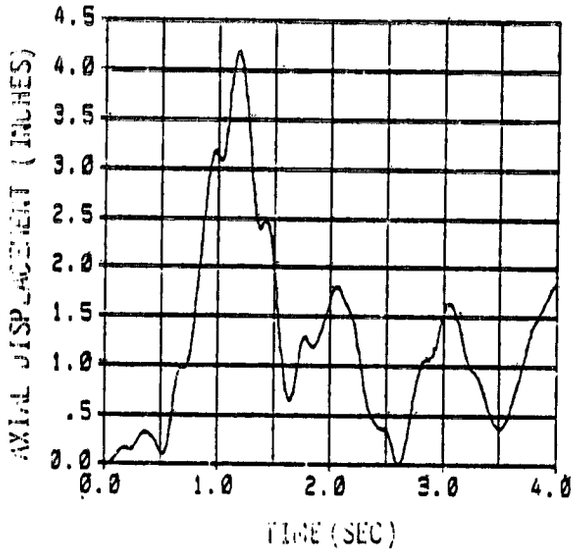

Figure 18 Wing Axial Displacement History for Typical Revenue Service Landing

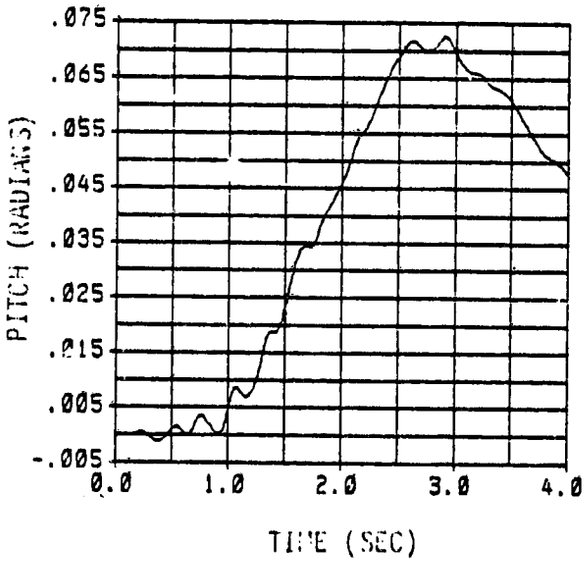

Figure 19 Wing Pitch History for Typical Revenue Service Landing

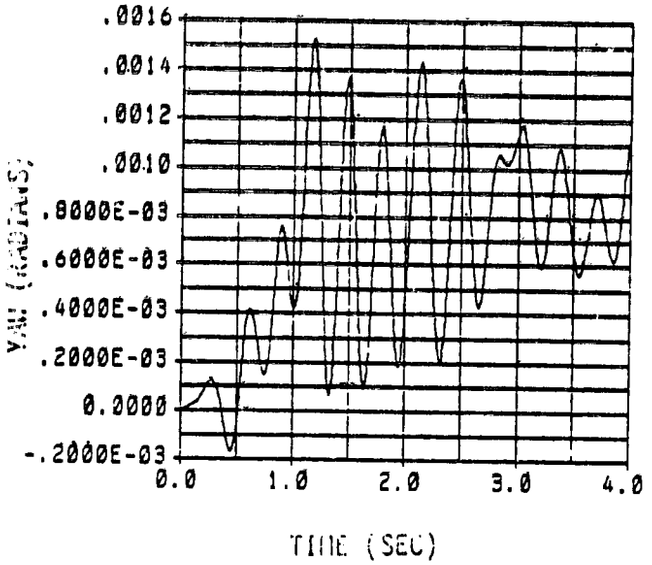

Figure 20 Wing Yaw History for Typical Revenue Service Landing

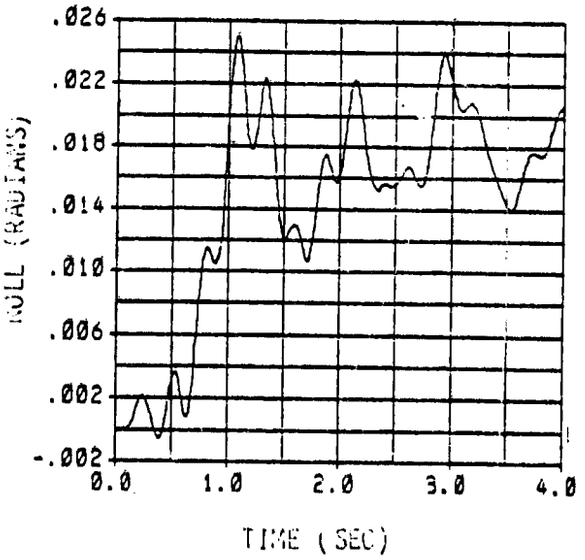

Figure 21 Wing Roll History for Typical Revenue Service Landing

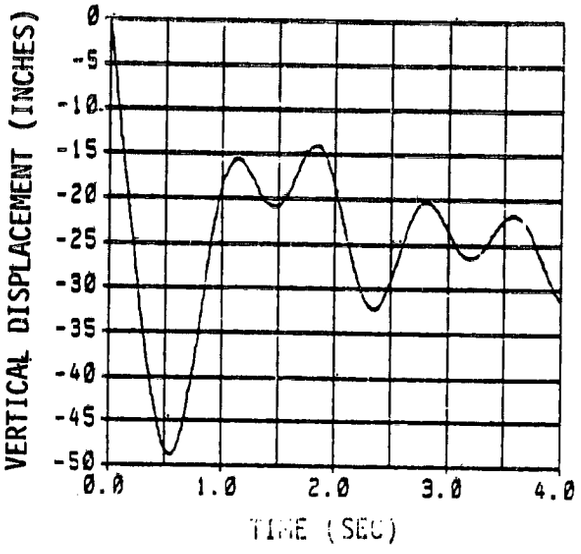

Figure 22 Wing Vertical Displacement History for Hard Landing

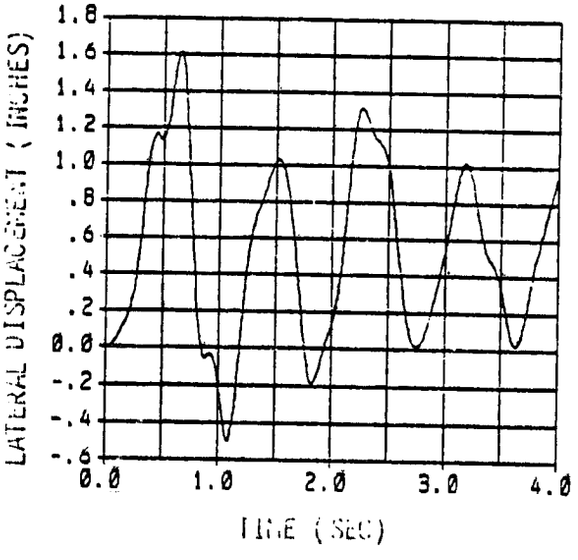

Figure 23 Wing Lateral Displacement History for Hard Landing

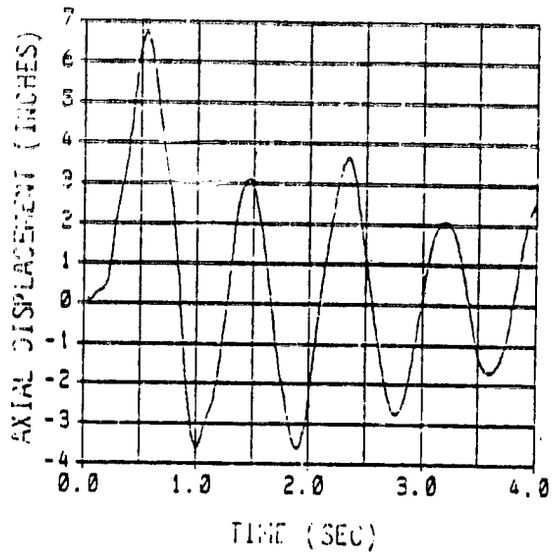

Figure 24 Wing Axial Displacement History for Hard Landing

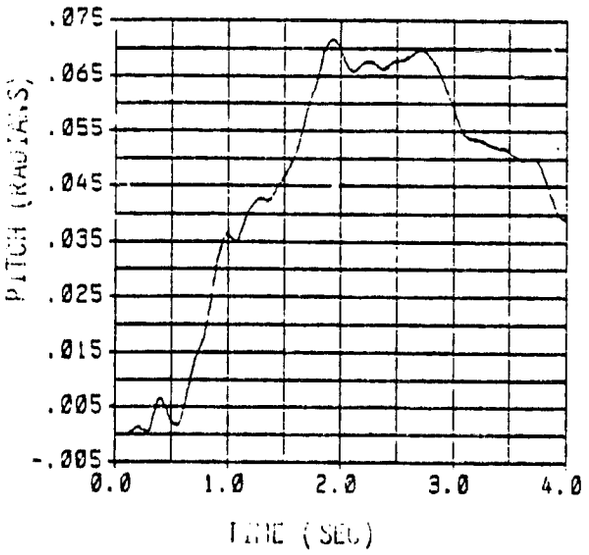

Figure 25 Wing Pitch History for Hard Landing

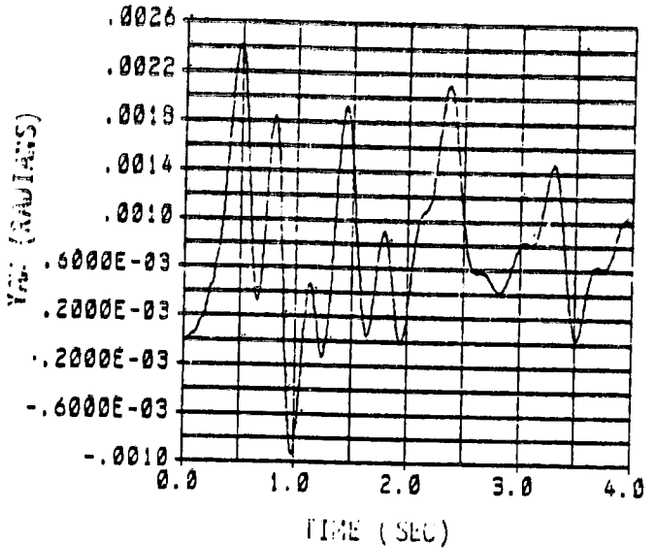

Figure 26 Wing Yaw History for Hard Landing

REPRODUCIBILITY OF THE
ORIGINAL PAGE IS POOR

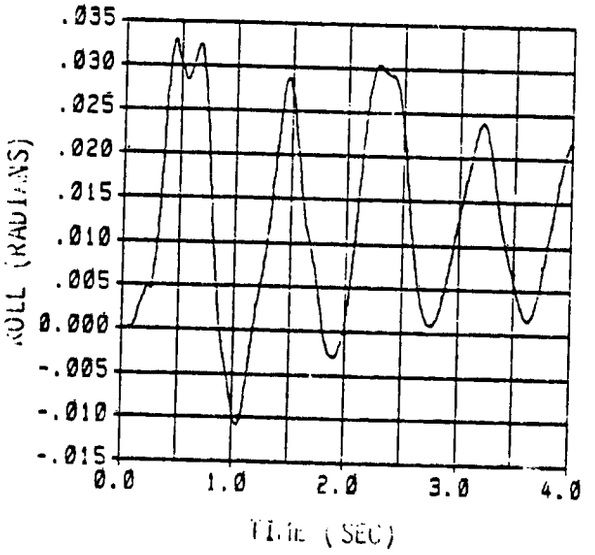

Figure 27 Wing Roll History for Hard Landing

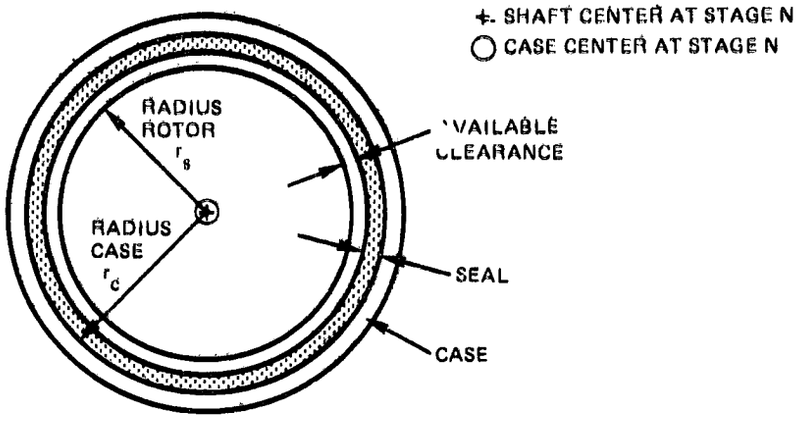

A. ROTOR/CASE UNDEFLECTED POSITION AT TIME = t_0

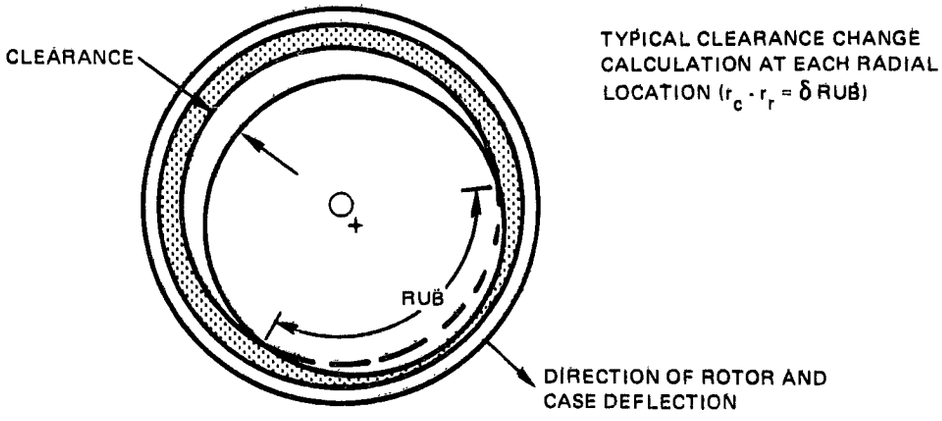

B. ROTOR/CASE DEFLECTED POSITION AT TIME = $t_0 + \Delta t$

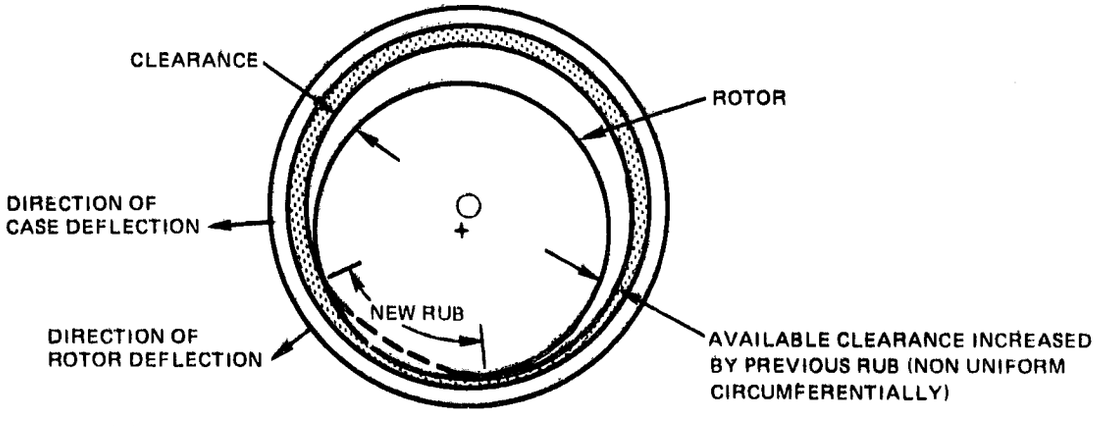

C. ROTOR/CASE DEFLECTED POSITION AT SUBSEQUENT TIME POINT

Figure 28 Dynamic Clearance Change Calculation Procedure

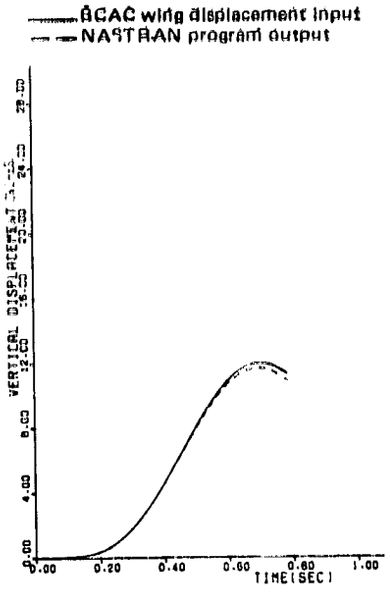

Figure 29 Wing Vertical Displacement Evaluation for Vertical Gust

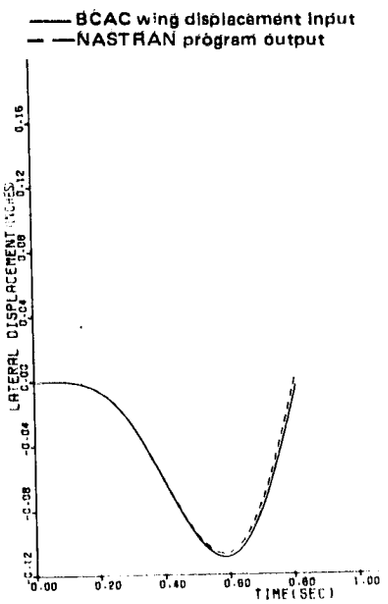

Figure 30 Wing Lateral Displacement Evaluation for Vertical Gust

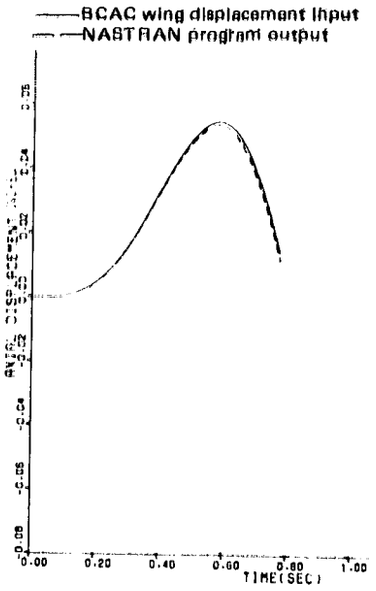

Figure 31 Wing Axial Displacement Evaluation for Vertical Gust

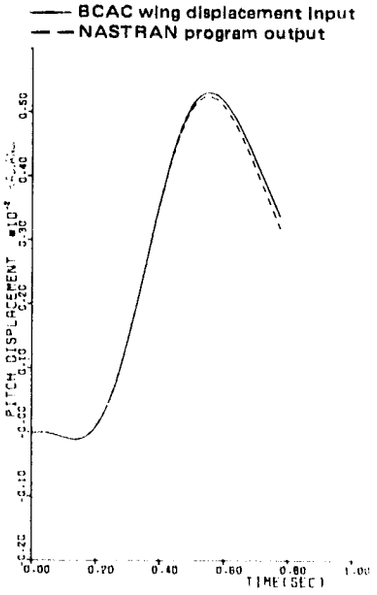

Figure 32 Wing Pitch Displacement Evaluation for Vertical Gust

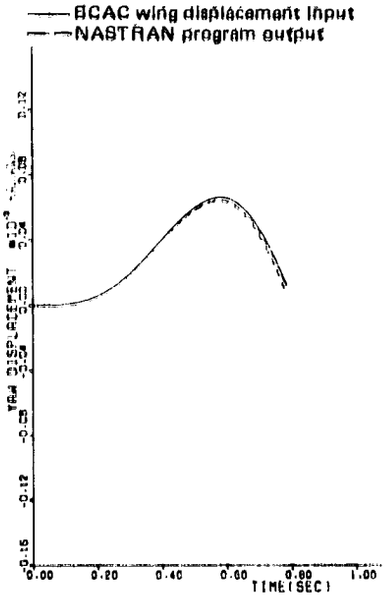

Figure 33 Wing Yaw Displacement Evaluation for Vertical Gust

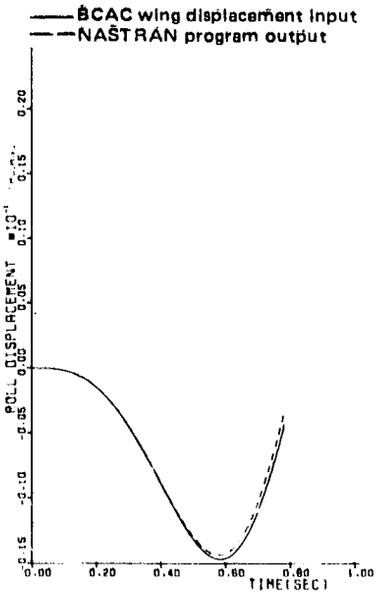

Figure 34 Wing Roll Displacement Evaluation for Vertical Gust

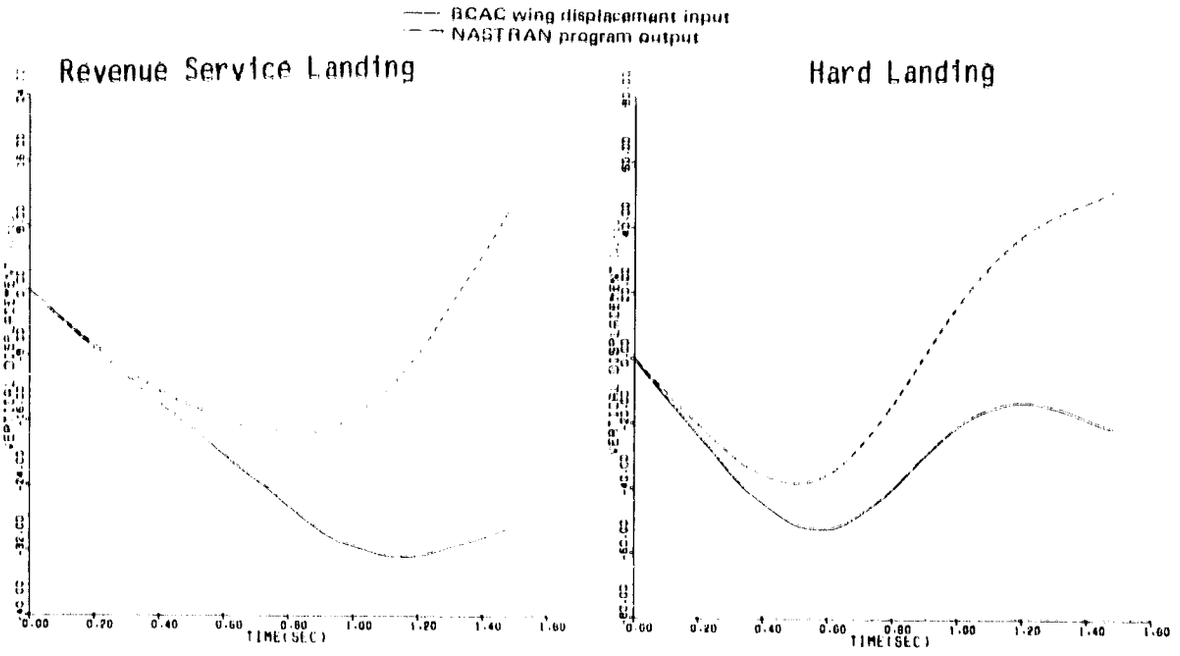

Figure 35 Wing Vertical Displacement Evaluation for Landing Events

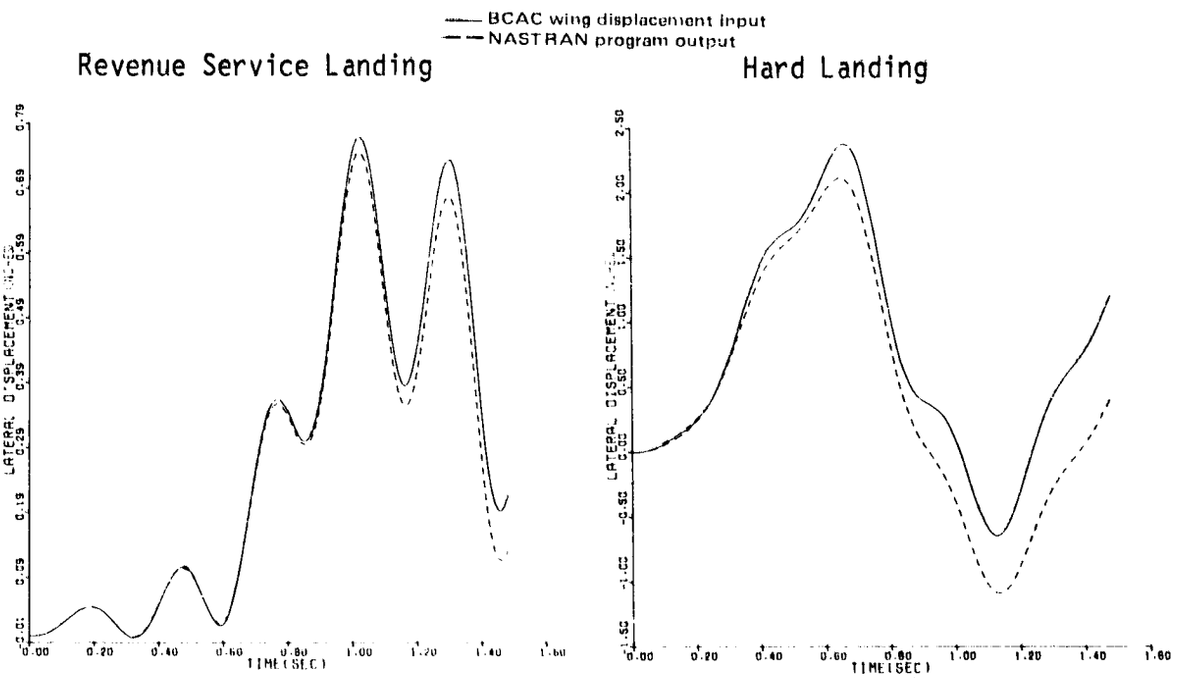

Figure 36 Wing Lateral Displacement Evaluation for Landing Events

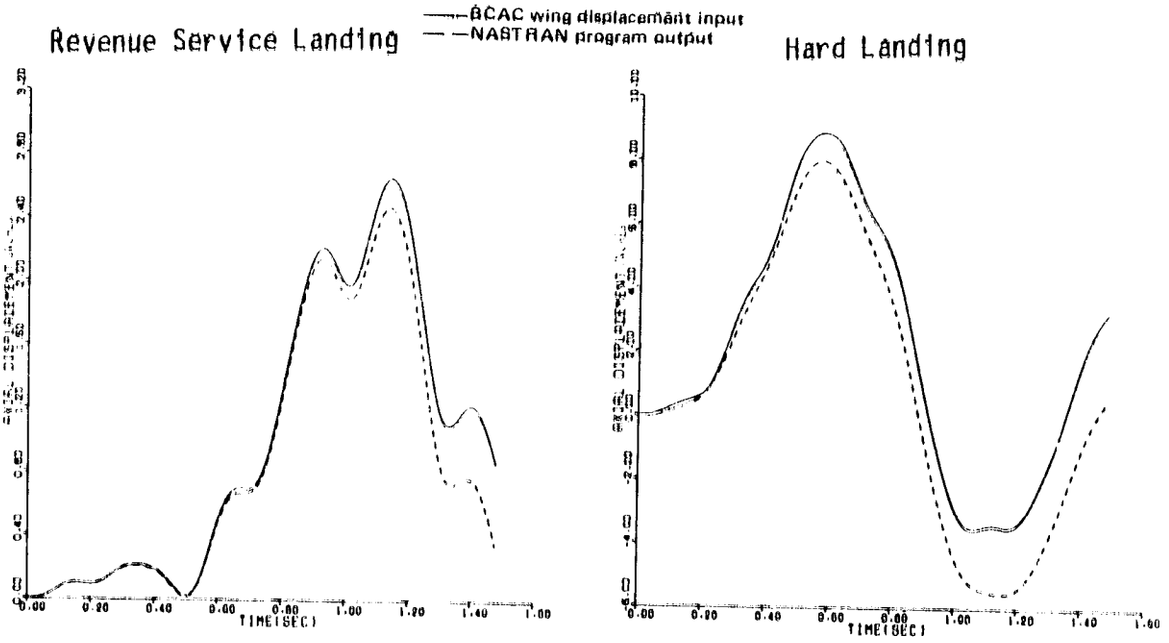

Figure 37 Wing Axial Displacement Evaluation for Landing Events

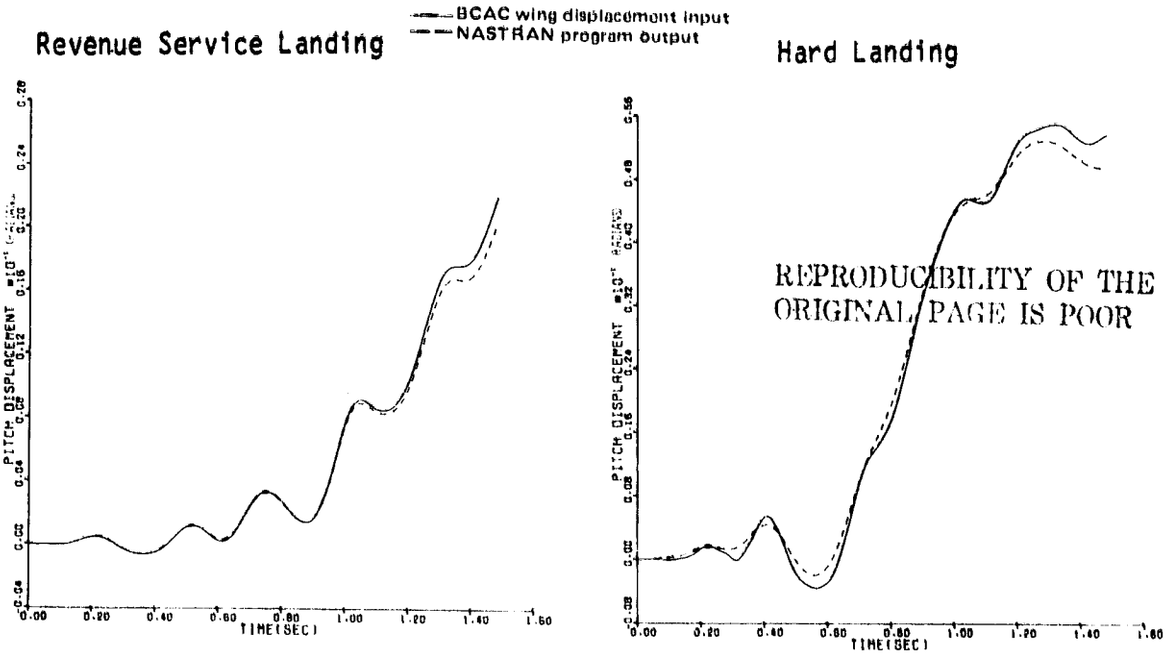

Figure 38 Wing Pitch Displacement Evaluation for Landing Events

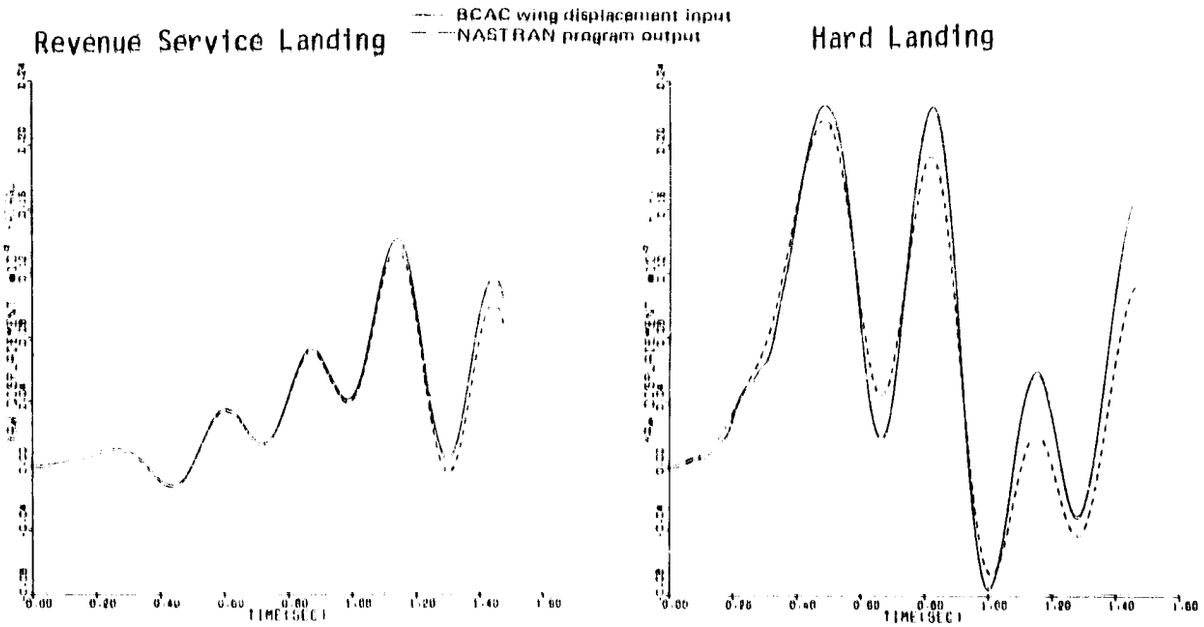

Figure 39 Wing Yaw Displacement Evaluation for Landing Events

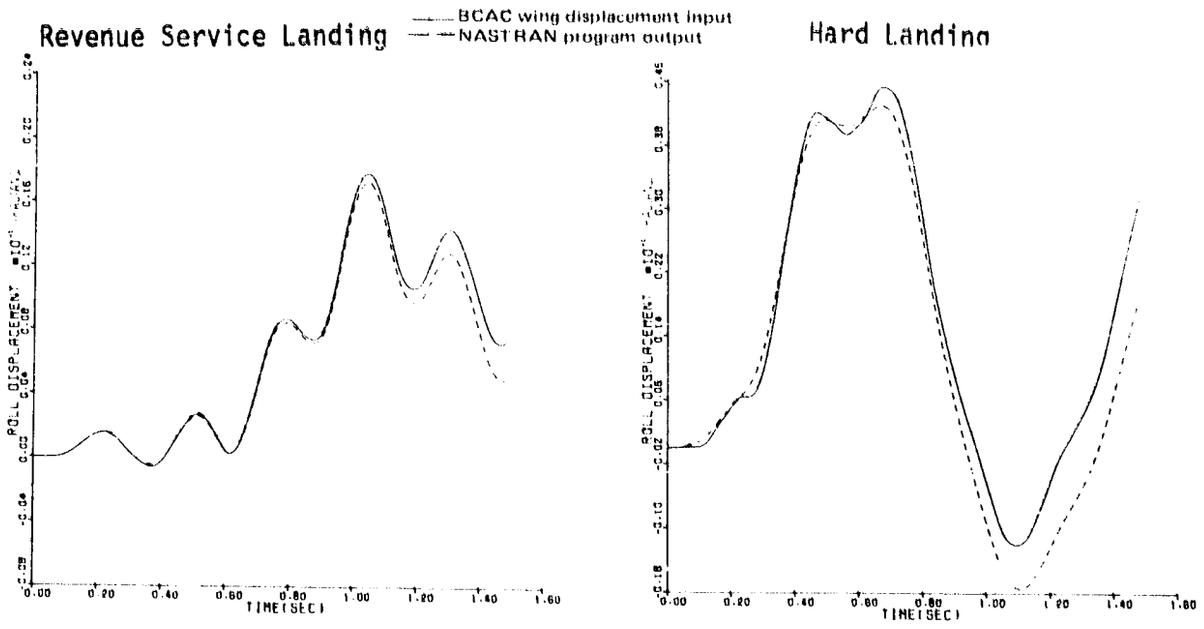

Figure 40 Wing Roll Displacement Evaluation for Landing Events

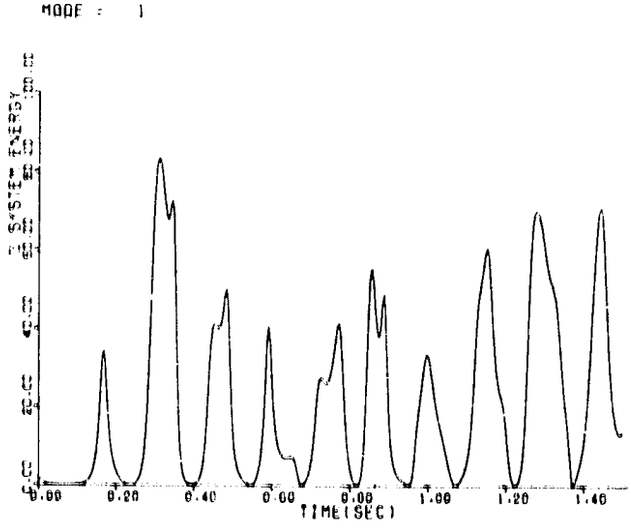

Figure 41 Energy Level Associated with Mode 1 for the Revenue Service Landing

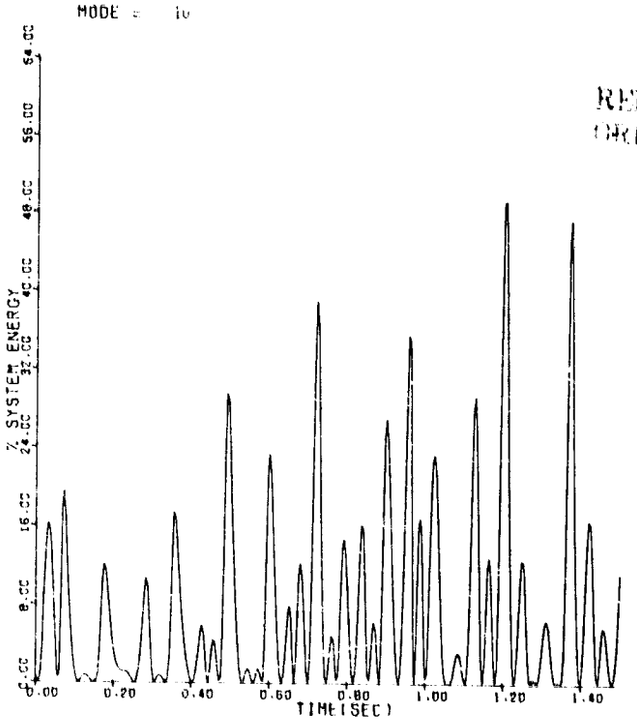

Figure 42 Energy Level Associated with Mode 10 for the Revenue Service Landing

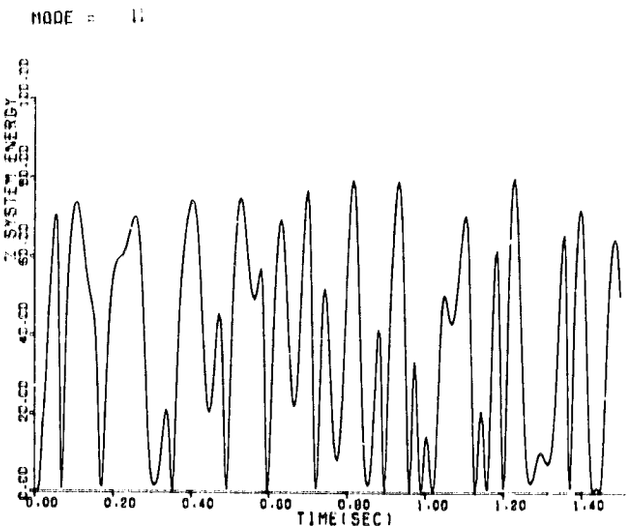

Figure 43 Energy Level Associated with Mode 11 for the Revenue Service Landing

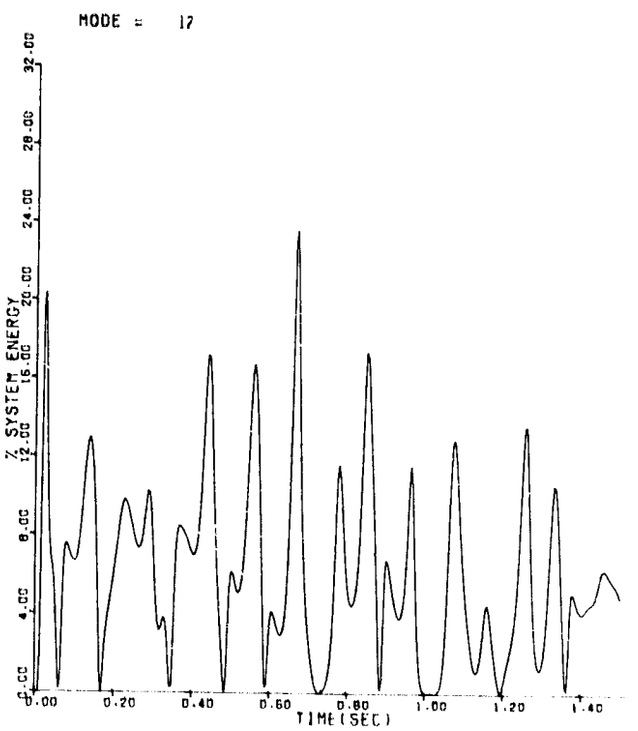

Figure 44 Energy Level Associated with Mode 12 for the Revenue Service Landing

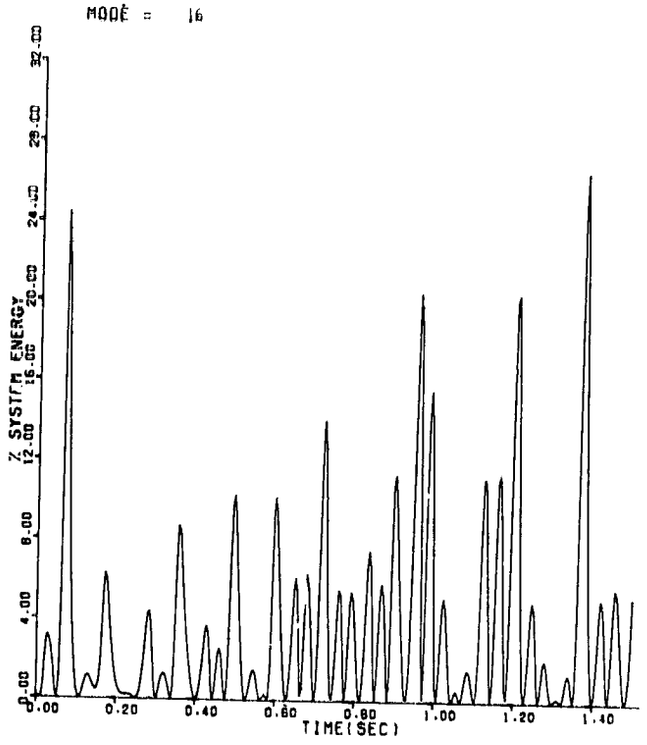

Figure 45 Energy Level Associated with Mode 16 for the Revenue Service Landing

APPENDIX

LIST OF SYMBOLS

A	=	Amplitude of mode
E	=	Elastic energy of system
g	=	Gravity
I	=	Mass moment of inertia of stage
M	=	Moment
N	=	Number of cycles
P_b	=	Substructure boundary displacements
P_I	=	Participation factors for various substructure fixed boundary modes
TSFC	=	Thrust specific fuel consumption
Δt	=	Incremental time step
ϕ	=	Rotation
Ω	=	Rotor rotational velocity
δ	=	Critical damping ratio
$\{\phi^c\}$	=	Displacement of internal degree of freedom due to boundary displacement, i.e., $\{\phi^c\} = -[K_{II}]^{-1} \cdot [K_{IB}]$
ω	=	Circular frequency
$[C]$	=	Structure viscous damping matrix
$[G]$	=	Rotor gyroscopic matrix
$[K]$	=	Structure stiffness matrix
$[\tilde{K}]$	=	Generalized stiffness = $[\tilde{\omega}^2]$
$[M]$	=	Structure mass matrix
$[\tilde{M}]$	=	Generalized mass = $[\tilde{I}]$
$[\phi]$	=	Zero speed modal matrix
$\{x\}$	=	Displacement vector (in)
$\{F(t)\}$	=	Forcing function (lbs)
$\{\eta\}$	=	Modal participation vector

Subscripts

A	=	Anti-symmetric
b	=	Boundary
e	=	Exact
f	=	Frequency
I	=	Internal
m	=	Modal
N	=	Normalized
n	=	N^{th} cycle
o	=	Initial
p	=	Polar
S	=	Symmetric
t	=	Time step size
x,y,z	=	Coordinate direction

Matrix Symbols

$[\ ]^T$	=	Matrix transpose
$[\ ]^{-1}$	=	Matrix inverse
$[\ddot{\ }]$	=	Acceleration
$[\dot{\ }]$	=	Velocity
$[\ \ ]$	=	Diagonal matrix